Mon. Not. R. Astron. Soc. **000**, 000–000 (0000) Printed 16 October 2015 (MN LATEX style file v2.2)

HEROIC: 3D General Relativistic Radiative Postprocessor with Comptonization for Black Hole Accretion Discs

Ramesh Narayan[1⋆] Yucong Zhu[1], Dimitrios Psaltis[2⋆], Aleksander Sądowski[3⋆]
[1] *Harvard-Smithsonian Center for Astrophysics, 60 Garden Street, Cambridge, MA 02138, USA*
[2] *University of Arizona, 933 N. Cherry Ave, Tucson, AZ 85721, USA*
[3] *MIT Kavli Instiatute for Astrophysics and Space Research, 77 Massachusetts Ave, Cambridge, MA 02139, USA*

arXiv:1510.04208v2 [astro-ph.HE] 15 Oct 2015

16 October 2015

ABSTRACT

We describe HEROIC, an upgraded version of the relativistic radiative post-processor code HERO described in a previous paper, but which now Includes Comptonization. HEROIC models Comptonization via the Kompaneets equation, using a quadratic approximation for the source function in the short characteristics radiation solver. It employs a simple form of accelerated lambda iteration to handle regions of high scattering opacity. In addition to solving for the radiation field, HEROIC also solves for the gas temperature by applying the condition of radiative equilibrium. We present benchmarks and tests of the Comptonization module in HEROIC with simple 1D and 3D scattering problems. We also test the ability of the code to handle various relativistic effects using model atmospheres and accretion flows in a black hole space-time. We present two applications of HEROIC to general relativistic MHD simulations of accretion discs. One application is to a thin accretion disc around a black hole. We find that the gas below the photosphere in the multi-dimensional HEROIC solution is nearly isothermal, quite different from previous solutions based on 1D plane parallel atmospheres. The second application is to a geometrically thick radiation-dominated accretion disc accreting at 11 times the Eddington rate. The multi-dimensional HEROIC solution shows that, for observers who are on axis and look down the polar funnel, the isotropic equivalent luminosity could be more than ten times the Eddington limit, even though the spectrum might still look thermal and show no signs of relativistic beaming.

Key words: methods: numerical – radiative transfer – accretion, accretion discs – black hole physics

1 INTRODUCTION

Comptonization plays a crucial role in determining the high-energy emission properties of a variety of astrophysical objects, e.g., X-ray emission from X-ray binaries (White et al. 1988; Ponman et al. 1990) and from active and quiescent galactic nuclei (see, e.g., Haardt & Maraschi 1991; Yuan & Narayan 2014, and references therein), nonthermal spectral properties of galactic microquasars (McClintock & Remillard 2006a; Done et al. 2007), cooling rates and decay timescales of X-ray bursters (Joss 1977), scattering by hot plasma clouds in intra-cluster media (Prokhorov et al. 2010). The ubiquity of hot ionized gas in astrophysical settings motivates the need for accurate treatment and modelling of the Compton scattering process.

In the case of black hole accretion discs, cold seed photons emitted from a thermal disc are upscattered by hot coronal electrons (Sunyaev & Titarchuk 1980), producing a whole host of spectral shapes in X-rays such as power-laws and Compton humps. Many systems, especially those in the low-hard spectral state, are observed with a dominant Compton component (Grove et al. 1998; Gierlinski et al. 1997; McClintock & Remillard 2006a), where interpretation of the data requires accurate modeling of the power-law tail. This is especially true in the case of reflection line modeling for black hole systems (Tanaka et al. 1995; Reynolds 2014), where slight errors in the continuum can lead to systematic biases in the derived black hole parameters (Haardt 1993).

Accurate analytic models of the Comptonized spectrum have been worked out during the last several decades for

⋆ E-mail: rnarayan@cfa.harvard.edu (RN); dpsaltis@email.arizona.edu (DP); asadowsk@mit.edu (AS)

© 0000 RAS

various regimes such as for optically thick, homogeneous 1D and 3D media (Sunyaev & Titarchuk 1980), at the limit of low electron energies (Haardt 1993), at the relativistic limit for optically thin media (Coppi & Blandford 1990), and for bulk Comptonization (see Turolla et al. 2002, and references therein). However, the complex nature of time-dependent simulations of accretion flows around black holes precludes the use of analytic models, motivating the development of numerical Comptonization schemes.

Monte-Carlo based methods have been a popular approach to the problem (Pozdnyakov et al. 1983; Gorecki & Wilczewski 1984; Stern et al. 1995; Dolence et al. 2009; Kawashima et al. 2012; Schnittman & Krolik 2013; Mościbrodzka et al. 2014) owing to the ease with which the technique can handle relativistic geometries and the complex angle and frequency dependent scattering process. The biggest drawback of the Monte-Carlo approach is that photon statistics limit the accuracy of the computations. This problem is worst in the limit of photon energies much higher than the injection energy, where there is a dearth of photons and hence poor photon statistics [1]. Monte Carlo methods also suffer in the limit of high optical depths – here, the full photon diffusion process is computationally very taxing, which in practice restricts MC-based codes to problems with only moderate optical depths ($\tau \lesssim 10$).

Another approach is to discretize the problem and numerically solve the radiative transfer problem for some preset fixed geometry (e.g., compPS: Poutanen & Svensson 1996 for moderate optical depths; compTT: Titarchuk & Lyubarskij 1995 for accretion discs; TLUSTY: for 1D atmospheres Hubeny et al. 2001; Zane et al. 1996 and Psaltis 2001 for bulk Comptonization). The main advantage of this approach is that it can easily handle optically thick problems via a Kompaneets operator approach, which uses a diffusion approximation to handle the nonrelativistic Comptonization problem. This approach is particularly amenable to the short characteristics fixed-grid framework of HERO (Hybrid Evaluator for Radiative Objects), a 3D GR radiation postprocessor code which we described in a previous paper (Zhu et al. 2015, hereafter Paper 1). Here we implement Comptonization in HERO and update the name of the code to HEROIC (HERO Including Comptonization). The primary advance in our work is that we introduce a self-consistent relativistic radiation module for the 3D Comptonization problem of hot accretion flows around black holes.

Regardless of the approach taken for solving the Compton problem, a final raytracing calculation is needed to connect the result to the actual spectral observations of astrophysical systems. Typically, geodesic paths are traced backwards from a distant observation plane until they hit the accretion flow (see, e.g., Rauch & Blandford 1994; Broderick & Blandford 2003; Dovčiak et al. 2004; Dexter & Agol 2009; Kulkarni et al. 2011; Psaltis & Johannsen 2012; Zhu et al. 2012). This yields a transfer function that allows one to map the local Comptonized disc emission to the spectrum as measured by the distant observer. In cases of high scattering optical depths, it is crucial for raytracing methods to resolve the complete nonlocal structure of the scattered radiation field (Schnittman & Krolik 2013). For Monte Carlo-based methods, this translates to a more computationally expensive "emitter-to-observer" paradigm since this is how the photon diffusion process works in nature (see Laor et al. 1990; Kojima 1991; Dolence et al. 2009; Schnittman & Krolik 2013 for a few recent codes that follow this philosophy). Grid based methods instead require a fully 3D treatment of the radiative problem accounting for all the nonlocal scattering terms in the emissivity profile. In the case of HEROIC, this is achieved by solving for the complete 3D scattered radiation field everywhere around and inside the disc before the raytracing process is initiated.

The organization of this paper is as follows. In §2 we describe the methodology used by HEROIC, focusing in particular on Comptonization; specifically, we explain how the ray evolution equation works in the presence of Compton scattering and how we solve it using a Kompaneets-based approach. We also describe how we solve self-consistently for the temperature of the radiating medium. This is followed in §3 with a series of 1D and 3D benchmark tests to verify the correct operation of the code. Then, in §4 we present two applications of HEROIC to data obtained with general relativistic magnetohydrodynamic (GRMHD) disc simulations. Finally, in §5 we conclude with a discussion.

2 METHODS

HEROIC solves the radiative transfer equation iteratively to obtain a steady state solution for the radiation intensity I_ν as a function of position $\mathbf{r}$, frequency ν and ray direction $\mathbf{n}$. If the problem requires it, HEROIC also applies the condition of radiative equilibrium to solve for the temperature of the gas in each grid cell. Other fluid quantities, specifically, the density ρ and four-velocity u^μ, are kept fixed. Thus, HEROIC solves the radiative transfer problem, but does not deal with the dynamics of the fluid. The latter should be specified as part of the initial setup, and would usually be obtained from a general relativistic radiation hydrodynamics or MHD simulation (e.g., Sądowski et al. 2014; McKinney et al. 2014; Fragile et al. 2014; Sądowski & Narayan 2015; Takahashi & Ohsuga 2015). HEROIC assumes that the system is time-steady. Therefore, it is best-suited for objects in steady state. If the code is applied to time-varying systems, then effectively one makes the "fast-light" approximation, i.e., one neglects time-travel delays between different regions of the source.

In a typical black hole accretion disc application, one assumes axisymmetry and solves the problem on a two-dimensional spatial grid in Boyer-Lindquist (polar) coordinates r-θ in the Kerr space-time of the black hole. At each grid point, the radiation field is decomposed over a uniform grid of angles, typically $N_A = 80$ angles, covering the full 4π steradians, and over a grid of frequencies, typically 10 frequencies per decade distributed uniformly in $\log\nu$. The intensities I_ν, the mean intensity,

$$J_\nu = \frac{1}{4\pi}\int I_\nu(\mathbf{n})\, d\Omega, \tag{1}$$

the opacity, the temperature, etc., are all described in the local comoving frame of the fluid. However, ray geodesics are best computed in the fixed spatial grid of the "lab" (Boyer-Lindquist) frame. Since we are using a form of the radiative

[1] The use of an energy-weighted scattering kernel is one workaround for the photon-starvation problem.

transfer equation that is relativistically invariant, transforming quantities from one frame to the other is straightforward.

2.1 Basic Equations

HEROIC solves the radiative transfer problem iteratively using the method of characteristics, as described in more detail in Paper 1.

The radiative transfer equation states that the intensity I_ν of a ray evolves along the ray trajectory according to

$$\frac{dI_\nu}{d\tau_\nu} = -I_\nu(\tau_\nu) + S_\nu(\tau_\nu), \tag{2}$$

where τ_ν is the optical depth at frequency ν measured along the ray and is given by

$$d\tau_\nu = (\kappa_\nu + \sigma_\nu)ds, \tag{3}$$

where κ_ν and σ_ν are the absorption and scattering coefficients and s is distance along the ray.[2] The quantity S_ν is the source function, which governs the rate at which energy is introduced into the beam, accounting for both intrinsic thermal emission and scattering. The formal solution of the radiative transfer equation (2) for the intensity $I_\nu(\tau_{\nu,2})$ at some location labeled by optical depth $\tau_{\nu,2}$ can be written in terms of the intensity $I_\nu(\tau_{\nu,1})$ at another location $\tau_{\nu,1} < \tau_{\nu,2}$ (i.e., located at some earlier point along the ray trajectory) and the source function between the two locations as follows:

$$I_\nu(\tau_{\nu,2}) = I_\nu(\tau_{\nu,1})e^{\tau_{\nu,1}-\tau_{\nu,2}} + \int_{\tau_{\nu,1}}^{\tau_{\nu,2}} S_\nu(\tau_\nu)e^{\tau_\nu-\tau_{\nu,2}}d\tau_\nu. \tag{4}$$

Paper 1 describes at some length how the code HERO uses the above formal solution to iteratively solve for the radiation field over the entire grid.

The inclusion of Comptonization in HEROIC introduces two changes relative to the discussion given in Paper 1. First, the source function now takes the form

$$S_\nu = \epsilon_\nu B_\nu + (1-\epsilon_\nu)J_{\nu,\mathrm{Compt}}, \tag{5}$$

where ϵ_ν is the ratio of absorption to total opacity,

$$\epsilon_\nu = \frac{\kappa_\nu}{\kappa_\nu + \sigma_\nu}, \tag{6}$$

$B_\nu(\tau_\nu)$ is the Planck function corresponding to the local temperature at location τ_ν, and $J_{\nu,\mathrm{Compt}}$, which in Paper 1 was simply equal to the mean intensity J_ν, now depends on the details of Compton-scattering. Specifically, if radiation with a local mean intensity distribution J_ν scatters once off the hot electrons in the Comptonizing medium, then $J_{\nu,\mathrm{Compt}}$ is the resulting intensity distribution.

For notational convenience later on, we rewrite the source function in terms of the uncomptonized J_ν by introducing an "amplification factor" a_ν,

$$S_\nu = \epsilon_\nu B_\nu + (1+a_\nu)J_\nu, \tag{7}$$

where we have absorbed all the complexities of Comptonization into a_ν. The latter is defined by the relation

$$J_{\nu,\mathrm{Compt}} \equiv A_\nu J_\nu \equiv \frac{1+a_\nu}{1-\epsilon_\nu}J_\nu, \tag{8}$$

where A_ν describes the boost factor in the radiation field at frequency ν due to Compton scattering. Note that Compton scattering mixes radiation at different frequencies, so the quantities A_ν and a_ν are functions not just of the post-scattering frequency ν but also of the pre-scattering frequency. Equations (7) and (8) are thus valid only if a_ν and A_ν are defined for a specific pre-scattering intensity distribution J_ν. This is not a limitation for our purposes since these quantities are constantly recomputed based on the current solution as the iterations in HEROIC proceed.

The second difference due to Comptonization is that, when evaluating the integral in equation (4), we find it necessary to expand $S_\nu(\tau_\nu)$ versus τ_ν up to at least the quadratic term:

$$S_\nu(\tau_\nu) = S_\nu(\tau_{\nu,2}) + S'_\nu(\tau_\nu - \tau_{\nu,2}) + \frac{1}{2}S''_\nu(\tau_\nu-\tau_{\nu,2})^2 + \cdots. \tag{9}$$

Quadratic order is helpful for any problem that has a source of heating or cooling which results in a transfer of energy from gas to radiation or vice versa. But it is particularly important in the case of Comptonization under very optically thick conditions, as we have found during the tests discussed in §§3.2, 3.3. In the work described in this paper, we have truncated the series at the quadratic term (Paper 1 stopped at the linear term). The evaluation of the coefficients S'_ν and S''_ν in equation (9) is discussed in §2.3.

Notice that the radiative transfer problem involves an intimate coupling between the intensities and the source function. Ray intensities are computed from the spatially varying source function via equation (4). However, the source function itself depends on the radiation field through $J_{\nu,\mathrm{Compt}}$, which depends on J_ν and $a_\nu(J_\nu)$, and is ultimately determined by the local intensities. Solving in parallel for the temperature only adds to the complexity. We use the lambda iteration technique with acceleration (§2.4) to solve the radiative transfer part of the problem, and have developed other techniques to solve for the temperatures (§2.5).

2.2 Compton Boost Factor

The Compton boost factor A_ν is locally defined and computed in each spatial cell. It describes the effect of Compton scattering by electrons with the temperature T of this cell[3] on the mean radiation intensity J_ν in the cell. Both T and J_ν change from one iteration to the next, so A_ν is computed afresh in each iteration.

HEROIC computes A_ν by solving for the evolution of the photon number density,

$$n_\nu = \left(\frac{c^2}{2h}\right)\frac{J_\nu}{\nu^3}, \tag{10}$$

as a result of scattering. The evolution is computed via the Kompaneets equation,

$$\frac{\partial n}{\partial t_{\mathrm{scatt}}} = f(\theta_e)\frac{1}{x^2}\frac{\partial}{\partial x}\left(x^4\left[\frac{\partial n}{\partial x} + n(n+1)\right]\right), \tag{11}$$

where t_{scatt} measures the characteristic time of the system

[2] Although, for simplicity, we have written the transfer equation here in non-relativistic notation, everything is done in a relativistically covariant form within HERO and HEROIC (see Paper 1 for more details).

[3] We do not distinguish between the electron temperature T_e and the gas temperature T_{gas}. We refer to both as T.

in units of the number of scattering events, θ_e is the dimensionless electron temperature,

$$\theta_e = \frac{kT}{m_e c^2}, \tag{12}$$

x is the dimensionless frequency,

$$x = h\nu/kT, \tag{13}$$

and the function $f(\theta_e) = \theta_e$ in the limit of non-relativistic temperatures, as originally considered by Kompaneets, but can be approximated at relativistic temperatures by

$$f(\theta_e) \approx \frac{(1 + 3.683\theta_e + 4\theta_e^2)}{(1 + \theta_e)}\,\theta_e, \tag{14}$$

as discussed in the Appendix.

We are interested in the radiation field $J_{\nu,\rm Compt}$ after a single scattering event. This corresponds to starting with an initial photon number density $n_{\nu,\rm initial}$ given by equation (10) for the current mean intensity J_ν, solving Equation (11) for the photon distribution $n_{\nu,\rm final}$ after a time $\delta t_{\rm scatt} = 1$, and computing from this the Compton boost factor,

$$A_\nu = \frac{J_{\nu,\rm final}}{J_\nu} = \frac{n_{\nu,\rm final}}{n_{\nu,\rm initial}}. \tag{15}$$

Due to the stiff nature of equation (11), we solve the partial differential equation using the approach described in Chang & Cooper (1970). The system is discretized along a logarithmic frequency grid and the photon fluxes in neighboring frequency bins are chosen such that the expected quasiequilibrium state for the given gas temperature and total photon number remains stationary. This guarantees convergence towards the expected thermal photon distribution, and guards against instabilities that can arise from the stiffness of the equation. Additionally, since the Kompaneets equation is a diffusion equation, the coupling is only between neighboring frequency bins, which results in a simple tridiagonal system that is easy to invert using standard methods. The boundary conditions are zero photon flux at the lower and upper frequency boundaries to ensure conservation of photon number:

$$\frac{\partial n}{\partial x} + n(n+1) = 0, \qquad x = x_{\rm min},\ x_{\rm max}. \tag{16}$$

The Chang & Cooper (1970) approach has been successfully tested and applied in other codes (Pomraning 1973; Madej 1989; Hubeny et al. 2001), with some implementations being more sophisticated than ours due to differences in the choice of interpolation scheme.

One detail is worth mentioning. When the scattering optical depth $\Delta\tau_{\rm scatt}$ across a spatial cell is large, the mean number of scatterings experienced by a photon as it moves across the cell, $n_{\rm scatt} \sim (\Delta\tau_{\rm scatt})^2$, can be much larger than unity. We have then found that it is better to evolve the Kompaneets equation over a time $t_{\rm scatt} = n_{\rm scatt}$ rather than $t_{\rm scatt} = 1$, and to correspondingly estimate A_ν from the output of the Kompaneets equation by

$$A_\nu = 1 + \frac{n_{\nu,\rm final}(x) - n_{\nu,\rm initial}(x)}{n_{\rm scatt}\, n_{\nu,\rm initial}(x)}. \tag{17}$$

The precise choice of $n_{\rm scatt}$ is not critical though we find that it is better to scale it with $(\Delta\tau_{\rm scatt})^2$ rather than $\Delta\tau_{\rm scatt}$. In HEROIC we use

$$n_{\rm scatt} = 1 + \Delta\tau_{\rm scatt} + (\Delta\tau_{\rm scatt})^2. \tag{18}$$

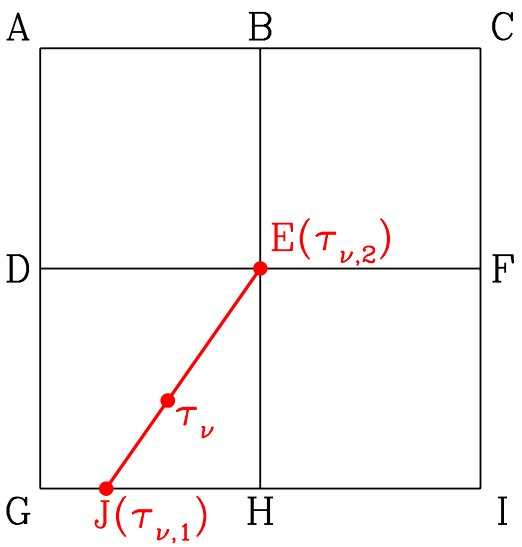

Figure 1. Schematic plot showing the ray geometry corresponding to the short characteristics method used in HEROIC. The point E is the reference cell, and its neighboring cells are A, B, C, D, F, G, H, I (in 2D geometry). Given a particular direction **n** along which one wishes to calculate the radiation intensity I_ν, one computes a null geodesic in the backward direction (the thick red line) until the geodesic intersects one of the neighboring cell boundaries, indicated by the point J. The radiative transfer equation (4) is integrated from the point J at optical depth $\tau_{\nu,1}$ to the point E at $\tau_{\nu,2}$. This is repeated for all ray directions **n** at E and for all frequencies ν, thereby building up an estimate of the radiation field at E.

The optical depth $\Delta\tau_{\rm scatt}$ is estimated by considering a typical trajectory through the cell. Again the precise choice is not important. One other detail: when the Compton y-parameter across the cell, which is roughly equal to $n_{\rm scatt}\theta_e$, becomes large, we limit $n_{\rm scatt}$ such that $y \sim$ few.

Since the Kompaneets equation is based on a Fokker-Planck approach, it is valid only when the change in the frequency of a photon in a single scattering is small. This condition breaks down at large temperatures. With $f(\theta_e) = \theta_e$, the solution deviates already at $kT_e \approx 20\,$keV, but with the generalized $f(\theta_e)$ given in equation (14) and discussed in the Appendix, one might be able to go up to 100 keV. In fact, the equation will continue to give smooth well-behaved solutions, and the solution will still have the right qualitative behavior, at even higher temperatures, only accuracy will be lost.

2.3 Quadratic Variation of the Source Function

In the presence of optically thick Comptonization, the radiative transfer solution behaves correctly only if we keep terms up to the quadratic order in the source function (9). In the context of the short characteristics method, the point $\tau_{\nu,2}$ in equation (4) corresponds to the particular cell where one is interested in computing the intensity of a ray, indicated by the point E in Figure 1, and $\tau_{\nu,1}$ corresponds to the point J on a neighboring cell boundary. The source function at E is known, and that at J is estimated by interpolating

between the known source functions at G and H. The series expansion (9) is then used to represent the source function at intermediate points such as that labeled τ_ν in the figure.

Given the source function at two boundary points ($\tau_{\nu,2}$, $\tau_{\nu,1}$), one can immediately obtain a linear approximation for $S_\nu(\tau_\nu)$ in between, and this was the approach taken in Paper 1. Obtaining a quadratic approximation is less straightforward, especially if we do not wish to involve additional neighboring cells in the estimate. We use the radiative transfer equation itself to estimate S''_ν. Differentiating equation (7) twice with respect to τ_ν, we have

$$\frac{d^2 S_\nu}{d\tau_\nu^2} \approx \frac{d^2(\epsilon_\nu B_\nu)}{d\tau_\nu^2} + (1+a_\nu)\frac{d^2 J_\nu}{d\tau_\nu^2}, \tag{19}$$

where we have ignored the variation of a_ν along the ray. To estimate the second derivative of J_ν we proceed as follows.

Following standard definitions in radiative transer theory (Mihalas 1978), the zeroth angular moment of the radiation field is J_ν as defined in eq. (1), and the first and second angular moments are

$$\mathbf{H}_\nu = \frac{1}{4\pi}\int I_\nu(\mathbf{n})\,\mathbf{n}\,d\Omega, \tag{20}$$

$$\mathbf{K}_\nu = \frac{1}{4\pi}\int I_\nu(\mathbf{n})\,\mathbf{nn}\,d\Omega, \tag{21}$$

where $\mathbf{n}$ is a unit vector along the direction of a ray, and $\mathbf{H}_\nu$ and $\mathbf{K}_\nu$ are related to the flux vector and the pressure tensor, respectively. By taking moments of the radiative transfer equation (2), one obtains

$$\nabla_\tau \cdot \mathbf{H}_\nu = -J_\nu + S_\nu, \tag{22}$$

$$\nabla_\tau \cdot \mathbf{K}_\nu = -H_\nu, \tag{23}$$

which gives the following second-order partial differential equation for $\mathbf{K}_\nu$,

$$\nabla_\tau^2 \mathbf{K}_\nu = J_\nu - S_\nu. \tag{24}$$

Here, the subscript τ in ∇_τ is to indicate that we are considering spatial gradients in terms of the optical depth τ_ν. In regions of large optical depth, the pressure tensor is expected to be diagonal and isotropic, so we write (this corresponds to the Eddington closure relation):

$$\mathbf{K}_\nu \approx \mathrm{diag}(J_\nu/3). \tag{25}$$

Equation (24) then gives

$$\nabla_\tau^2 J_\nu = 3(J_\nu - S_\nu) = -3(\epsilon_\nu B_\nu + a_\nu J_\nu). \tag{26}$$

As our final approximation, we assume that the second derivative of J_ν with respect to τ_ν is isotropic, which then gives the relation we seek,

$$\frac{d^2 J_\nu}{d\tau_\nu^2} \approx -\epsilon_\nu B_\nu - a_\nu J_\nu. \tag{27}$$

Substituting this in equation (19) and neglecting the second derivative of $\epsilon_\nu B_\nu$, we finally obtain

$$S''_\nu \equiv \frac{d^2 S_\nu}{d\tau_\nu^2} \approx -\epsilon_\nu B_\nu - a_\nu S_\nu. \tag{28}$$

This expression, which involves no derivatives and can be evaluated locally in each cell, is used in HEROIC for estimating S''_ν. Once we have $S_\nu(\tau_{\nu,2})$, $S_\nu(\tau_{\nu,1})$ and $S''_\nu(\tau_{\nu,2})$, we can immediately estimate $S'_\nu(\tau_{\nu,2})$ by making use of equation (9).

A number of approximations were made en route to deriving equation (28), but they are all harmless. The inclusion of the quadratic term S''_ν is important only in optically thick, highly Comptonized regions, and in these regions we believe the terms we have retained are the important ones. In principle, we could avoid some of the approximations, e.g., we could retain the term $d^2(\epsilon_\nu B_\nu)/d\tau_\nu^2$ in equation (19), though this would require using information from neighboring cells, or we could avoid the Eddington approximation (eq. 25) and instead work directly with the pressure tensor $\mathbf{K}_\nu$ (which HEROIC does compute in each cell during each iteration). But we have not found such refinements necessary in the work we have done so far.

2.4 Accelerated Lambda Iteration

The algorithm used by HEROIC to solve the radiative transfer problem is Lambda Iteration, but enhanced with a simple form of acceleration. The basic Lambda Iteration (LI) algorithm is straightforward and goes as follows. At the end of iteration n, given the current estimate of the source function S_ν^n as well as the current estimates of the opacity coefficients, κ_ν^n, σ_ν^n, ϵ_ν^n (corresponding to the current estimate of the local temperature) in all the cells, new intensities for the $(n+1)$th iteration are computed via equation (4) (for all ray directions at all frequencies in all cells, see Fig. 1)). From these intensities, the new J_ν^{n+1} is obtained and the Kompaneets equation is solved in each cell to obtain a_ν^{n+1}. Combined with the new B_ν^{n+1} corresponding to the current temperature, this enables one to compute $S_{\nu,\mathrm{LI}}^{n+1}$ via equation (7), where the subscript LI is to indicate that this estimate corresponds to LI. If needed, temperatures are updated at this point, thus completing one iteration of LI.

In the presence of strong scattering, especially when the scattering optical depth τ across a cell is large, LI is very slow to converge, requiring of order τ^2 iterations. The solution is to use Accelerated Lambda Iteration (ALI, see Hubeny 2003 for a short review of the method). Formally, the LI steps described above may be viewed as a mapping between the new mean intensities J_ν^{n+1} in the various cells and the previous source functions S_ν^n. The mapping is linear and may be formally written via a Λ operator,

$$J_\nu^{n+1} = \Lambda(\{S_\nu^n\}), \tag{29}$$

where it must be stressed that Λ is not a local relation within a single cell but couples all cells via the radiative transfer equation. If the Λ matrix can be inverted, then one could achieve very rapid convergence to the solution. However, in practice, the Λ matrix is too large and difficult to invert directly, so an approximate operator Λ^* is used instead.

The simplest approximation, the one we use, is to consider only the diagonal components of the Λ operator, motivated by the fact that the diagonal terms usually dominate the system. These terms represent the contribution of S_ν^n in a given cell to J_ν^{n+1} in the same cell, the "self-illumination contribution" to the source term. Thus we rewrite the Λ mapping as follows

$$J_\nu^{n+1} = \lambda_\nu^n S_\nu^n + \Lambda'(S_\nu^n), \tag{30}$$

where now λ_ν^n is a number (not a matrix) associated with a single cell and frequency, J_ν^{n+1} and S_ν^n correspond to the same cell and frequency, and the final Λ' term represents

the remaining non-local part of the Λ operator that couples information from other cells. Using the above relation, the updated $S^{n+1}_{\nu,\rm LI}$ from LI can be written as

$$\begin{aligned} S^{n+1}_{\nu,\rm LI} &= \epsilon^{n+1}_\nu B^{n+1}_\nu + (1+a^{n+1}_\nu) J^{n+1}_\nu \\ &= \epsilon^{n+1}_\nu B^{n+1}_\nu + (1+a^{n+1}_\nu)\lambda^n_\nu S^n_\nu \\ &\quad +(1+a^{n+1}_\nu)\Lambda'(\{S^n_\nu\}). \end{aligned} \tag{31}$$

In the ALI scheme, S^n_ν in the middle term on the right hand side is replaced with S^{n+1}_ν and this term is brought over to the left hand side. Solving the resulting equation for S^{n+1}_ν then gives the ALI estimate for the new source function:

$$S^{n+1}_{\nu,\rm ALI} = S^n_\nu + \frac{(S^{n+1}_{\nu,\rm LI} - S^n_\nu)}{[\,1-(1+a^{n+1}_\nu)\lambda^n_\nu\,]}. \tag{32}$$

The factor in the denominator in the last term is generally smaller than unity, which means that the shift in the source function from one iteration to the next is larger (sometimes much larger) than with basic LI. This results in accelerated convergence[4]. Note that all the quantities except λ^n_ν on the right hand side of equation (32) are available at the end of each iteration of LI, and λ^n_ν itself can be easily computed as follows.

From equation (30) it is seen that, for each cell and frequency, $\lambda^n_\nu = \partial J^{n+1}_\nu/\partial S^n_\nu$ while keeping all the other source function terms constant (i.e., keeping the Λ' term constant). Therefore, in parallel with the regular LI calculation, we carry out a second intensity calculation where, for each ray in equation (4), we set $I_\nu(\tau_{\nu,1}) = S_\nu(\tau_{\nu,1}) = 0$ and $S_\nu(\tau_{\nu,2}) = 1$. We recompute the Taylor series (9) for these values of the two source functions, using the appropriately modified S''_ν. The resulting J^{n+1}_ν directly gives λ^n_ν.

As discussed earlier, the particular ALI approach described here focuses just on the self-illumination term and thereby avoids inverting the full Λ matrix. This is a very good approximation for the spatial part of the problem because ALI is needed most when the scattering optical depth across a single cell is large, and it is precisely in this limit that the exponentials in (4) ensure that the intensity is dominated by the local source function. On the other hand, the decomposition in equation (30) also isolates frequencies from one another and it is not a good approximation to assume that the self-illumination term dominates in frequency space, where the primary effect of Comptonization is to move radiation from one frequency to another.

We find that HEROIC with the simple version of ALI described here requires more iterations to converge when tackling a problem involving Comptonization than for an identical problem with only Thomson scattering. On the other hand, ALI still gives much faster convergence than simple LI. As a final comment, the coupling of frequencies in the Λ matrix could be incorporated into equation (30) by making λ^n_ν itself a matrix that couples neighboring frequencies over a stencil size of order the frequency dispersion of the Kompaneets operator. We have not found it necessary to experiment with such refinements. In rare circumstances, usually when the Compton y-parameter across a cell is very large, ALI can be unstable. In these cases, it necessary to switch back to ordinary LI.

[4] For greater stability, we usually replace $(1+a^{n+1}_\nu)$ by $(1-\epsilon_\nu)$ in equation (32), thereby reverting to ALI without Comptonization (see paper 1). Although this slows down the rate of convergence, it makes the code more robust.

2.5 Solving for the Temperatures

The methods described so far are sufficient to obtain a solution to the radiation problem, provided the temperature, or equivalently B_ν, is given in each cell. This is the case for the test problems described in §3. However, in the applications discussed in §4, and for many future applications of HEROIC, we will not know in advance the temperatures in individual cells but will need to solve for them.

In a typical accretion disc problem, one will obtain for each cell, say from a GRMHD simulation, the density ρ, the four-velocity u^μ, the temperature T' (the prime here is to indicate that this is the temperature as determined by the simulation, which we will improve as part of solving the radiative transfer problem), and the heating rate per unit volume Q^+ (erg cm^{-3}s^{-1}). This last quantity is the rate at which thermal energy is added to the gas by viscous dissipation. For now, let us ignore energy advection and assume that Q^+ is equal to Q^-, the rate at which energy is transferred from gas to radiation per unit volume:

$$Q^- = Q^+. \tag{33}$$

This relation can be applied in each spatial cell in the grid, and this set of equations can be used to solve for the temperature. Details are given below.

There are two ways of estimating the cooling rate Q^- from the radiative transfer solution. First, we can take a microscopic approach in which we sum up all the intensity added to the radiation field through thermal emission or Compton scattering, and subtract from this all the intensity removed by absorption and scattering. The result, suitably integrated over frequency and angles, is obviously the net cooling rate of the gas. This gives

$$Q^- = 4\pi \int_\nu [\kappa_\nu(B_\nu - J_\nu) + \sigma_\nu(A_\nu - 1)J_\nu]\, d\nu, \tag{34}$$

where the factor of 4π is to go from "per steradian" to the "whole sphere". All the quantities on the right are known at each iteration of the radiative transfer algorithm and therefore it is possible to estimate Q^- for every cell.

The second estimate of Q^- comes from the spatial divergence of the radiation flux $\mathbf{F}$, where the latter can be written in terms of $\mathbf{H}_\nu$ (eq. 20) by

$$\mathbf{F} = 4\pi c \int_\nu \mathbf{H}_\nu d\nu. \tag{35}$$

The energy conservation equation of the radiation field then becomes

$$Q^- = \nabla_r \cdot \mathbf{F}, \tag{36}$$

where the subscript r on ∇_r is to indicate that the divergence is computed in spatial coordinates and not optical depth as in §2.3.

The two estimates of Q^- given in equations (34) and (36) are guaranteed to be driven towards each other as the radiation solution converges (subject to accuracy limitations due to the gridding of the problem). Therefore, we could substitute either of these estimates in equation (33) when solving for the temperature. The best strategy in our experience

is to use equation (34) in optically thin regions and equation (36) in optically thick regions and to transition smoothly between the two zones (the precise details do not seem to matter), very much in the spirit of the Lucy-Unsold method citepmihalas78. A motivatation this choice is that, in the optically thick regime, the opacities are large and B_ν and J_ν are also very large, but their difference is small. Therefore, the overall integral in equation (34) is much smaller than the values of the individual terms. Consequently, equation (36) provides a more accurate method for calculating Q^-.

Whichever version of Q^- we substitute in equation (33), we need to solve the resulting (coupled) non-linear set of equations for the temperatures. In optically thin regions, where we use equation (34), a Newton-Raphson-like approach is sufficient, but optically thick regions are more difficult. In the latter regions we use the form of Q^- given in equation (36), which ultimately takes the form of the Laplace equation for the pressure tensor (see eq. 24). We have had some success using acceleration schemes such as the successive over-relaxation (SOR) method (Press et al. 1992) to solve this strongly spatially coupled problem. However, note that the entire problem — radiation plus temperature — is often very involved and requires many iterations (hundreds to thousands), so one does not gain much by accelerating the temperature solution. Simple-minded local corrections to the temperature are frequently sufficient and converge to the correct temperature solution by the time the Comptonized radiative transfer problem has converged.

We now discuss the relativistic generalization of the above equations. The quantities Q^+, Q^- and all the terms in the right-hand side of equation (34) are defined in the local comoving fluid frame. Therefore, when we use this version of Q^-, relativity introduces no modifications. Equation (36) is more troublesome since the divergence operator is best handled in the lab (Boyer-Lindquist) frame and it is necessary to write the energy conservation equation of radiation in the latter frame. The time component of the energy-momentum conservation law for radiation takes the form (see Sądowski et al. 2013; Sądowski & Narayan 2015)

$$(R^\mu_0)_{;\mu} = -G_0, \tag{37}$$

where R^μ_ν is the stress-energy tensor of the radiation and G_ν is the radiation four-force. Both quantities are easily evaluated in the orthonormal fluid frame, where all our radiation quantities like J_ν, B_ν, κ_ν, a_ν, etc. are defined. In particular, the fluid-frame radiation four-force has time component $\widehat{G}_0 = -Q^-$, which is the energy transferred from the radiation to the gas, and the spatial components of the four-force are similarly the momentum components transferred from radiation to gas. Once $\widehat{R}^\mu_\nu$ and $\widehat{G}_\nu$ are computed in the fluid frame, one transforms these tensors and vectors to the lab frame and then substitutes the appropriate components into equation (37). This is the relativistic generalization of equation (36).

Finally, we discuss the issue of energy advection. Equation (33) is valid only for radiatively efficient flows where the gas immediately radiates whatever heating it experiences. In the more general situation, there is an additional entropy advection term in the energy equation and we have

$$Q^- = Q^+ - \rho T \frac{ds}{dt} = Q^+ - \frac{\rho k T}{\bar{m}} \frac{d}{dt}\left(\ln \frac{T^n}{\rho}\right). \tag{38}$$

Here d/dt represents a Lagrangian time derivative following a fluid element, $\bar{m}$ is the mean mass per particle in the fluid, and $n = 1/(\Gamma - 1)$ is the polytropic index of the gas. This is a nonrelativistic version of the equation.

Since d/dt is a Lagrangian time derivative, we can rewrite equation (38) in four-notation as

$$Q^- = Q^+ - \frac{c}{R_g}\left(\frac{n\rho k}{\bar{m}} u^\mu T_{;\mu} - \frac{kT}{\bar{m}} u^\mu \rho_{;\mu}\right), \tag{39}$$

where the additional factor of c/R_g is to convert from gravitational units used in typical GRMHD simulations to physical units; here $R_g = GM/c^2$, where M is the mass of the black hole (or other central gravitating object). Specializing further to Boyer-Lindquist coordinates, assuming steady state (no time dependence of quantities) and axisymmetry (no ϕ dependence), and replacing semicolons by commas since T and ρ are scalars, we obtain:

$$Q^- = Q^+ - \frac{nck\rho}{\bar{m}R_g}\left(u^r T_{,r} + u^\theta T_{,\theta}\right) + \frac{ckT}{\bar{m}R_g}\left(u^r \rho_{,r} + u^\theta \rho_{,\theta}\right). \tag{40}$$

This is the form of the energy equation (rather than eq. 33) that HEROIC uses when solving for temperatures. In practice, it makes a difference only in regions where the gas has a tendency to be advection-dominated, e.g., the plunging region of an accretion flow inside the ISCO (see Zhu et al. 2012) or the funnel region where a jet may be present.

2.6 Long Characteristics and Ray Tracing

The letter H in the name of the code HERO described in Paper 1 stands for Hybrid and refers to the fact that the code combines several stages: an initial stage in which the problem is solved using a short characteristics solver, a second stage in which the solution is improved using a long characteristics solver, and a final stage in which ray tracing is done to compute observables for a distant observer.

In the case of HEROIC, all the discussion so far was related to the short characteristics method. Unfortunatley, we do not yet have a long characteristics solver that can handle Comptonization. We do, however, have the ray tracing code that was already developed for HERO (Paper 1), and the same code can be used even when there is Comptonization. This is because the short characteristics solver obtains a solution for the source function S_ν and the temperature T (which allows one to calculate opacities). This is all that one needs for ray-tracing, since the latter involves nothing more than integrating equation (4) backwards from a distant observer over a grid of impact parameters and frequencies.

3 NUMERICAL TESTS

We have validated our Compton module in HEROIC by applying it to two test problems that admit analytic or quasi-analytic solutions. For these test problems, we considered the case of pure scattering with no absorption. We also carried out other tests to check some relativistic aspects of the code.

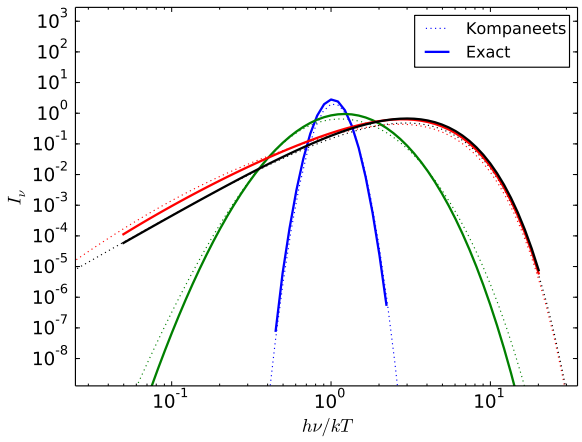

Figure 2. Comparison of numerical results obtained with the Kompaneets solver employed in HEROIC (§2.2) with the exact analytical solution (Eq. 41), for the spectral evolution of an initial delta-function at frequency $x = h\nu/kT = 1$. The different colors correspond to different values of the Compton y-parameter: 0.1 (blue), 1 (green), 10 (red), 100 (black). The slight deviations are largely because the initial distribution in the numerical solution is not a perfect delta-function but has a finite width equal to the size of a frequency bin.

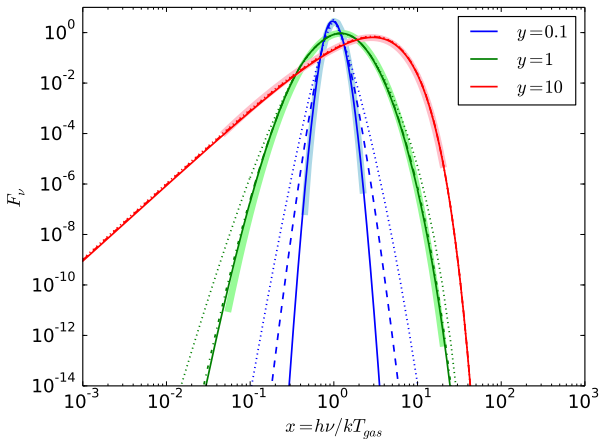

Figure 3. Comparison of numerical results from the Kompaneets solver with the analytical result for different frequency resolutions. The dotted, dashed and solid lines correspond to 10, 40 and 160 bins per frequency decade, respectively. The thick solid lines show the analytical solutions (Eq. 41).

3.1 Kompaneets Solver

We begin by benchmarking the Kompaneets solver, which is the workhorse that HEROIC relies on to handle all Comptonization problems. Consider the "Green's function" of an initially monoenergetic distribution of photons (delta-function in ν) as it evolves in energy via Compton scattering within a closed box of hot thermal electrons. If we ignore the nonlinear n^2 term in the Kompaneets equation (11), the problem is simple enough that an analytical solution is available in terms of complex integrals of the Whittaker functions $W_{k,m}(x)$ (Becker 2003):

$$f_G(x,y) = \frac{32}{\pi} e^{-9y/4} x_0^{-2} x^{-2} e^{(x_0-x)/2} \times \int_0^\infty e^{-u^2 y} \frac{u \sinh(\pi u)}{(1+4u^2)(9+4u^2)} W_{2,iu}(x_0) W_{2,iu}(x) du + \frac{e^{-x}}{2} + \frac{e^{-x-2y}}{2} \frac{(2-x)(2-x_0)}{x_0 x}, \quad (41)$$

where $x = h\nu/kT$ is the dimensionless frequency, $f_G(x,y)$ represents the Green's function spectral response of the system to a delta source injected at frequency x_0 after it has evolved over a timescale corresponding to a Compton $y = 4\theta_e n_{\rm scatt}$.

Figure (2) compares numerical solutions from our Kompaneets solver (§2.2) to the above analytical solution for different choices of y. In these calculations, we initialized HEROIC with a photon distribution that is non-zero in a single frequency bin at $x = x_0 = 1$. The numerical solutions from HEROIC agree very well with the analytical solution.

The minor discrepancies seen in Figure 2 are primarily due to the fact that the initial frequency distribution is not a perfect delta-function but has a finite width due to the bin size. This finite size slightly fattens the numerical Kompaneets result. Figure 3 shows the effect of changing the frequency resolution. We see that with increasing frequency resolution the agreement steadily improves. But even a resolution of 10 frequencies per decade (our default) is sufficiently accurate for most purposes since the deviations are noticeable only deep in the wings and that too only for a delta-function (the radiation sources we deal with generally do not have such narrow spectral distributions).

3.2 Plane Parallel Comptonizing Atmosphere

A typical Comptonization problem involves both spatial diffusion and Compton-scattering in frequency. Here we consider a simple problem in which we have a one-dimensional, plane parallel, hot, scattering atmosphere with a finite optical depth $2\tau_0$ through it. We assume steady injection of soft photons with a blackbody spectrum at the mid-plane. The injected photons random-walk away from the mid-plane, and their energies become modified with each scattering. We are interested in the steady state spectrum of the escaping radiation from the two surfaces.

Using the Kompaneets solver that was tested in the previous sub-section, we first calculate the correct solution to this model problem. For this, we need to compute the photon escape time distribution, where by time we mean the number of scatterings experienced by a photon before it escapes. A convolution of the photon escape time distribution with the Kompaneets derived spectrum for each escape time then yields the emergent spectrum for the problem.

Figure 4 shows an example of the spectral evolution of a $T_{\rm rad} = 10^4 K$ initial radiation field as it scatters in a thermal gas with $T = 10^6 K$. This set of spectra constitutes the "Compton kernel" which we will use for calculating the emergent spectrum from a Comptonizing atmosphere.

To calculate the escape time distribution for a 1D plane-

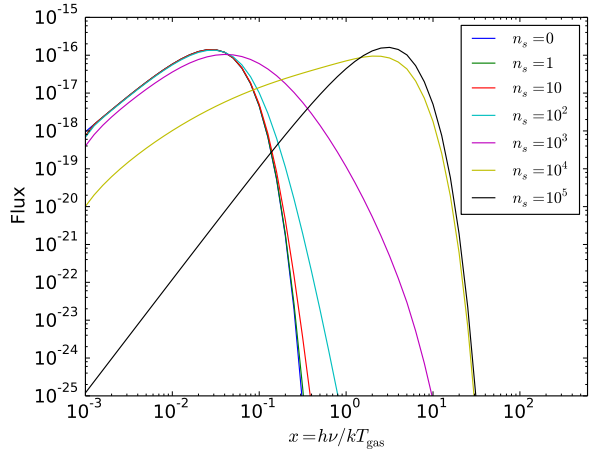

Figure 4. Sample Compton kernels computed with the Kompaneets solver. The problem considered is the Comptonization of an initial $T = 10^4 K$ radiation field that is upscattered by hot gas with $T = 10^6 K$. The different curves show Comptonized spectra after various numbers n_s of scattering events.

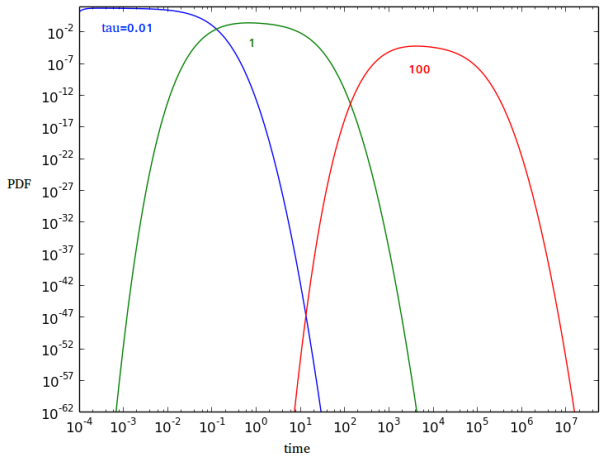

Figure 5. The escape time probability distribution function for various choices of plane parallel slab thickness. The escape time is measured in units of the characteristic scattering time. Note that the diffusion time scales with optical depth as $t \sim \tau$ in the optically thin limit and as $t \sim \tau^2$ in the optically thick limit.

parallel atmosphere, we solve the diffusion equation, i.e.

$$\frac{\partial n}{\partial t} = \frac{1}{3}\frac{\partial^2 n}{\partial \tau^2}, \tag{42}$$

where the factor of 1/3 is because we are considering diffusion of photons in three dimensions[5], τ is the perpendicular optical depth in the atmosphere, and t is measured in units of the number of scattering times. We initialize the system with a spatial delta-function distribution of photons at the mid-plane. We then allow the system to evolve and calculate the escaping photon number flux at the surface as a function of time. This flux, normalized by the number of initial photons, directly gives the escape time probability distribution.

Instead of taking the approach of Sunyaev & Titarchuk (1980), who tackle the diffusion problem analytically via series expansions, we opt for a numerical solution. We consider the upper half of the slab, and apply a reflecting boundary condition at the midplane because of symmetry. At the surface, for simplicity, we use the boundary condition appropriate to the two-stream approximation:

$$\left.\frac{\partial n}{\partial \tau}\right|_{\rm surf} + \sqrt{3}\, n|_{\rm surf} = 0. \tag{43}$$

Figure 5 shows the calculated distributions of escape times for a few values of τ. Convolving these with the Compton kernel shown in Figure 4 then gives the energy spectra of the escaping photons as a function of frequency. The results are shown by the dotted lines in Figure 6 for model atmospheres of various optical depths. The temperature of the scattering atmosphere is taken to be 10^6 K, and the photons injected at the mid-plane have a blackbody distribution with a temperature of 10^4 K.

Having computed the correct solutions, we solved the same problem using HEROIC. We used a logarithmically spaced spatial grid of 101 points, with 20 points for each decade of optical depth. In order to be consistent with the boundary condition (43) we used only two angles, and we used 61 frequencies distributed uniformly in $\log \nu$ from $\nu = 10^{12}$ Hz to 10^{18} Hz. We treated the midplane as a reflecting boundary with an additional steady source of blackbody radiation with temperature $10^4 K$. At the outer surface of the atmosphere, we assumed that there is no ingoing radiation. Since the temperature of the gas in the atmosphere is given ($T = 10^6$ K), there is no need for the temperature solution methods described in §2.5.

The resulting spectra obtained with HEROIC are shown by the solid lines in Figure 6. A comparison of these with the true solutions (dotted lines) shows that the agreement is quite good. Note that this is a comprehensive test of Comptonization at nonrelativistic temperatures since it includes all the elements described in §§2.2, 2.3 and 2.4. It is, however, a one-dimensional problem, whereas HEROIC was developed principally for multi-dimensional problems.

3.3 Spherical Scattering Atmosphere

Here we consider a homogeneous spherical Comptonizing atmosphere where photons are injected at the center and diffuse outwards. This problem is identical to the plane parallel previously discussed, except that it now occurs in spherical geometry. The corresponding diffusion equation is (Sunyaev & Titarchuk 1980):

$$\frac{\partial n}{\partial t} = \frac{1}{3}\frac{1}{\tau^2}\frac{\partial}{\partial \tau}\left(\tau^2 \frac{\partial n}{\partial \tau}\right). \tag{44}$$

We inject photons at the center (in practice at a radius $r_{\rm min} = 10^{-4} r_{\rm max}$) and solve the diffusion problem numerically for different radial optical depths τ_0. This gives us the escape time probability distributions. The central boundary condition is still set as reflection at $r = r_{\rm min}$ (to simulate the symmetry at the origin), while the outer boundary condition becomes modified to (see Sunyaev & Titarchuk 1980

[5] This coefficient is also compatible with the two-stream approximation for radiative transfer (Rybicki & Lightman 1979)

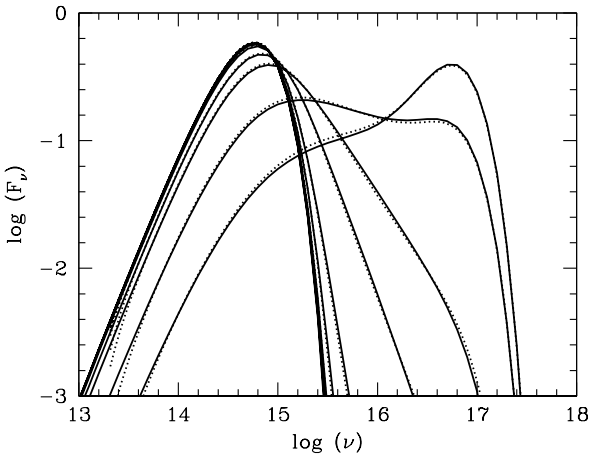

Figure 6. Spectra of the emergent radiation in the 1D plane parallel Compton scattering problem. Blackbody radiation with a temperature of 10^4 K is injected at the midplane of the slab and the scattering electrons are assumed to have a temperature of 10^6 K. From left to right as measured by the positions of the peak, the scattering optical depths to the midplane of the slab are: τ = 0, 1, 2, 3, 6, 10, 20, 30, 60, 100, respectively. Solid lines represent results obtained with (1D) HEROIC using two rays (which corresponds to the 2-stream approximation) and dotted lines represent exact results computed as described in the text.

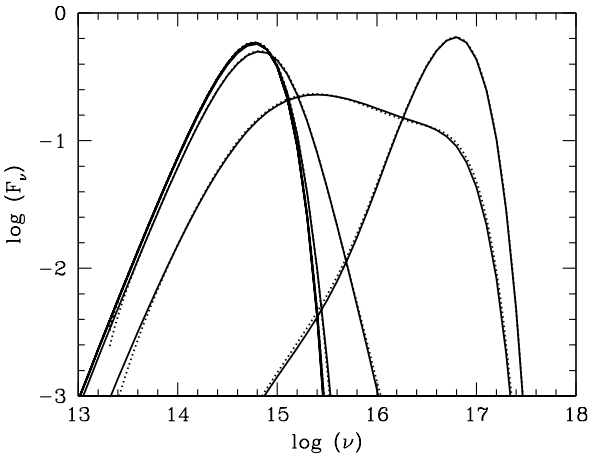

Figure 7. Same as figure 6, but for a 3D spherical diffusion problem. The injected radiation temperature and the scattering electron temperature are 10^4 K and 10^6 K respectively. From left to right in the position of the peak, the radial scattering optical depth of the spherical atmosphere is τ = 0, 1, 3, 10, 30, 100, 300, respectively. Solid lines represent results obtained with 2D axisymmetric HEROIC using 80 angles and dotted lines represent exact results.

– Appendix A):

$$\left.\frac{\partial n}{\partial \tau}\right|_{\rm surf} + \frac{3}{2}\, n|_{\rm surf} = 0. \qquad (45)$$

As before, we calculate the escape time probability distribution by solving the diffusion equation numerically and we then convolve this with the Compton kernel to compute the energy spectrum of escaping photons. The dotted lines in Figure 7 show the results. Note that the spectra are qualitatively quite similar to those for the 1D problem (Fig. 6), but the 3D spherical diffusion problem has on average shorter escape times compared to an equivalent 1D plane parallel problem with the same scattering depth. This is a simple consequence of the geometry – the mean distance to the surface is shorter in the 3D case. The shorter escape times in the spherical case translate to less strongly Comptonized spectra, as can be seen by comparing the dotted lines in Figures 7 and 6 for the same optical depth.

We solved the above 3D spherical problem independently using HEROIC. We assumed axisymmetry and solved for the radiation field in the 2D poloidal plane in spherical coordinates r, θ (there is no GR in this problem). The numerical grid consisted of 61 cells in radius distributed uniformly in $\log r$ from $r_{\rm min} = 3$ to $r_{\rm max} = 300$, and 31 points distributed uniformly in θ. The radiation field was solved on 80 angles distributed uniformly in direction (see Paper 1 for details) and 61 points in frequency exactly as in the 1D problem. To be consistent with the choice of a constant diffusion coefficient in Equation (44), the scattering sphere was taken to have a constant scattering opacity. The solid lines in Figure 7 show the results. We see that the agreement with the true spectra (dotted lines) is as good as in the plane parallel case. This test shows that Comptonization in HEROIC works correctly in multiple dimensions.

It should be noted that the short characteristics method used for these calculations has a serious ray defect in spherical coordinates, for which Paper 1 developed an approximate fix. Although this fix mitigates the error by a large factor, it is imperfect. In particular, the luminosity as a function of radius in a spherical problem is not constant (see Fig. 17 in Paper 1 and also Fig. 8 below). In the context of the present Comptonization test problem, the ray defect results in the photon luminosity (photons per second) escaping at $r = r_{\rm max}$ being somewhat less than the luminosity injected at $r = r_{\rm min}$. For the spectra shown by solid lines in Figure 7, we have normalized the escaping spectra by a correction factor so that the net photon luminosity is the same as in the corresponding model solutions (dotted lines). The energy spectra were not adjusted in any other way, so the very good agreement in the shapes of the spectra is a strong test of the algorithm used in HEROIC.

3.4 Gravitational Redshift

HEROIC is designed to work in relativistic spacetimes, and Paper 1 described a number of tests to verify that that HERO correctly handles ray propagation in vacuum. The tests included light-bending, gravitational redshift and Doppler shift. In this and the following subsection, we consider non-vacuum tests.

Figure 8 shows results corresponding to radiation propagating in a homogeneous scattering atmosphere in a Schwarzschild spacetime. For this test, we assume that a spherical surface at radius $r_{\rm min} = 2.2GM/c^2$ (where M is the mass) radiates as a blackbody with "temperature-at-

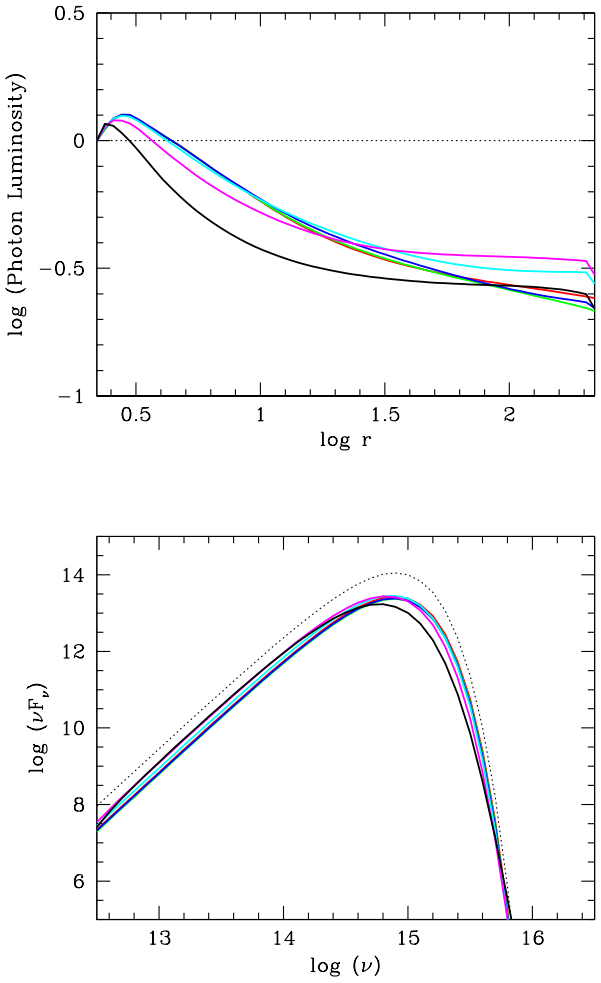

Figure 8. Top: Radial photon luminosity (photons/sec) normalized to the injected luminosity at the inner edge ($r_{\rm min} = 2.2$), as a function of radius r (in units of GM/c^2), for different choices of the radial scattering optical depth: $\tau = 1$ (red line), 3 (green), 10 (blue), 30 (cyan), 100 (magenta), 300 (black). Bottom: Corresponding spectra of the escaping radiation at the outer edge ($r_{\rm max} = 100\, r_{\rm min}$).

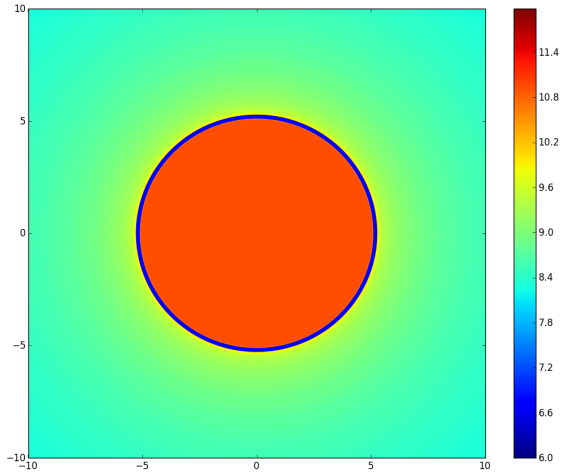

Figure 9. Ray-traced image of the model corresponding to $\tau = 1$ in Figure 8. The solid red region shows radiation escaping directly from the inner surface of the grid ($r = r_{\rm min}$), attenuated by $\exp(-\tau)$. The yellow-green-cyan regions show scattered radiation from the scattering atmosphere. Since $r_{\rm min}$ lies inside the photon orbit, the apparent size of the inner radiating surface is equal to that of the photon orbit ($r_{\rm photon,app} = \sqrt{27}$), shown by the blue circle.

infinity" of 10^4 K, i.e., with a local temperature, $T_{\rm surface} = 10^4{\rm K}/[1 - (2GM/c^2 r_{\rm min})]^{1/2} = 3.32 \times 10^4$ K, and that the radiation propagates through a uniform spherical scattering atmosphere (no absorptive opacity) extending from $r = r_{\rm min}$ up to $r = r_{\rm max} = 100 r_{\rm min}$. We vary the radial optical depth τ_0 of the atmosphere over a wide range of values up to a maximum of $\tau_0 = 300$. The atmosphere is at rest in the lab frame and it is cold, so there is no Comptonization. (We are not aware of any good test problems involving Comptonization in relativistic spacetimes.)

We use HEROIC to solve for the radiation field on a grid of 61 logarithmically spaced points in r and 31 uniformly spaced points in θ, assuming axisymmetry. We use 80 angles and 61 frequencies distributed uniformly in $\log \nu$ from $\nu = 10^{12}$ Hz to $\nu = 10^{18}$ Hz. The upper panel in Figure 8 shows the photon luminosity as a function of radius in the solutions obtained with HEROIC for different choices of τ. Notice that the luminosity is not constant with radius. This is because of the ray defect discussed in the previous subsection. A comparison with Figure 17 in Paper 1 shows similar features, viz., a drop in the luminosity over the first factor of several in radius, after which the luminosity remains constant. There are two differences in the present test. First, we now have a scattering atmosphere, not vacuum, so this test verifies that the approximate correction for the ray defect that was described in Zhu et al. (2015) works also in the presence of scattering. Second, the inner radius here is close to the horizon and well inside the photon orbit. This means that the majority of rays in the innermost region are pulled in towards the horizon and only a few rays propagate to larger radii. HEROIC is not handicapped by such extreme ray deflections.

The second aspect of this test is to check the spectrum of the radiation that emerges from the outer edge of the atmosphere and to verify that it does correspond to a blackbody at 10^4 K. The lower panel in Figure 8 shows the results. As already mentioned, the emerging flux is lower than expected, causing all the calculated spectra (solid lines) to lie below the theoretically expected spectrum (dotted line). However, the shapes are correct. The only exception is the model with the largest $\tau = 300$ where the spectrum (black line) is a little cooler than it should be. In this last case, the radiation effectively scatters $\sim \tau^2 \sim 10^5$ times before emerging at the surface. This test shows that the code is able to preserve spectra while propagating through optically thick media in a background with variable gravitational redshift.

Figure 9 shows the image of this scattering atmosphere

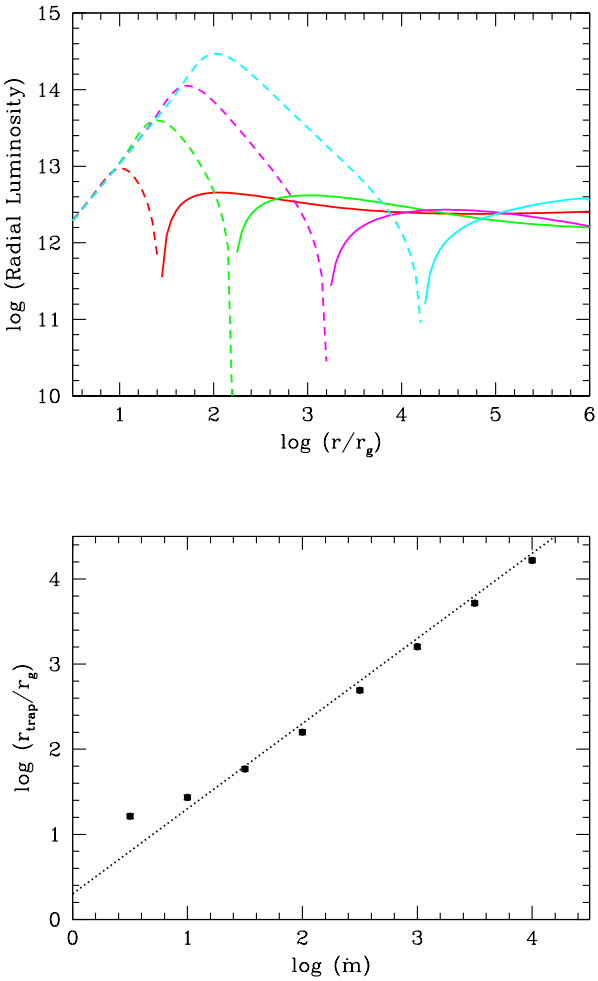

Figure 10. Top: Radial photon luminosity (photons/sec) in arbitrary units vs radius in units of r_g for spherical Bondi accretion as in Turolla et al. (2002). Four models are shown, corresponding to Eddington-scaled mass accretion rates of $\dot{m} = 10$ (red), 10^2 (green), 10^3 (magenta), 10^4 (cyan). Dashed line segments correspond to negative luminosities, where radiation is trapped by the accreting gas and is dragged into the center, and solid line segments correspond to positive luminosities, where radiation flows outward. The transition between the two corresponds to the trapping radius $r_{\rm trap}$. Bottom: Variation of $r_{\rm trap}$ with $\dot{m}$. Note the linear dependence once $\dot{m} \gg 1$.

as seen by a distant observer for the model with $\tau = 1$. The bright inner surface, attenuated by a factor of $\exp(-\tau)$ by scattering, is seen at the center, surrounded by faint emission from the extended scattering atmosphere. The apparent size of the inner surface agrees well with the theoretically expected radius of $\sqrt{27}GM/c^2$, the apparent size of the photon orbit (blue circle).

3.5 Radiation Trapping, Bulk Comptonization

Apart from gravitational redshift and ray deflections, Doppler effects play an important role in radiative transfer. The effect we are interested in here is the advection of radiation by an optically thick medium. Recall that, in HEROIC, the radiation field is described in the comoving frame of the fluid, while the radiative transfer computation is done entirely in the lab frame. If the fluid moves with respect to the lab frame, the dragging or advection of radiation by the moving fluid must ultimately result from Doppler modifications of the radiation intensity and frequency in the lab frame. We test this aspect of HEROIC.

The problem we consider is spherical accretion in a Schwarzschild background. We consider super-Eddington accretion rates so that radiation is trapped within a certain trapping radius $r_{\rm trap}$ and is dragged to the center. Any radiation outside the trapping radius is able to escape to infinity. We model this problem as closely as possible using the setup described in Turolla et al. (2002). The accreting gas has both (grey) absorption and scattering, whose magnitudes are tuned such that for all models the "absorption radius" $r_a = 5M$ and the "crossing radius" $r_c = 3.6M$, as in Turolla et al. (2002, note that their unit of length is $2M$, not M). For the opacity index n we choose the middle of the three values they considered: $n = 4$.

Figure 10 shows results obtained with HEROIC for various choices of the Eddington-scaled mass accretion rate $\dot{m}$. These models were computed on a 2D grid with 114 cells distributed logarithmically in radius, going from $r = 10^{0.35}M$ to $r = 10^6 M$, and 21 cells distributed uniformly in θ; the models assume axisymmetry (as in all the previous spherical tests), and use 80 angles and 61 frequencies. The upper panel shows the radial luminosity profiles as measured in the lab frame for $\dot{m} = 10,\ 10^2,\ 10^3,\ 10^4$. Dashed segments correspond to negative luminosities, i.e., the radiation here is trapped in the accreting gas and dragged inward. The radius at which the luminosity changes sign is the trapping radius $r_{\rm trap}$. The lower panel shows the variation of $r_{\rm trap}$ with $\dot{m}$ for a series of models. Except for small values of $\dot{m}$, where the inner absorbing boundary has an effect, we see that $r_{\rm trap}$ is quite accurately proportional to $\dot{m}$ (Begelman 1979). This indicates that HEROIC captures radiation trapping quite well. In the case of large values of $\dot{m}$, when the trapping radius is quite far out, the Doppler shifts that describe radiation advection are fairly small, but the code has no difficulty.

Radiation trapping is a v/c effect. A more difficult effect to capture is bulk Comptonization, which occurs when radiation propagates through a converging flow (like the Bondi flow). Figure 11 shows spectra of escaping radiation as calculated with HEROIC using the same setup as described above. For these calculations it is assumed that the accreting gas has a temperature of 10^4 K so that there is virtually no thermal Comptonization. In the absence of bulk Comptonization the spectrum of the escaping radiation should be a perfect blackbody, as in Figure 8. What we see instead are spectra that are blackbody-like at frequencies below the peak, but are distinctly power-law in shape at higher frequencies. The high energy power-law is the result of bulk Comptonization. However, the slopes appear to be too steep;

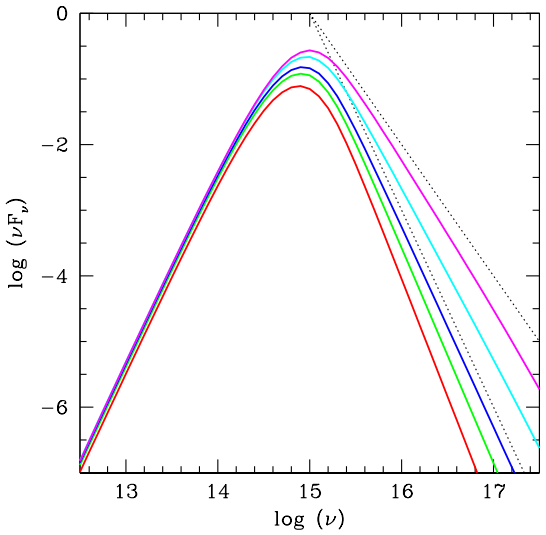

Figure 11. Spectra of escaping radiation for the Bondi accretion problem (Fig. 10) for $\dot{m} = 1$ (red), 2 (green), 3 (blue), 6 (cyan), 10 (magenta). Note the power-law tails at large frequencies (in contrast to the spectra in the bottom panel of Fig. 8). These power-laws are produced by bulk Comptonization. The two dotted lines correspond to photon indices of 4 (upper) and 5 (lower).

the photon indices Γ we obtain with HEROIC are larger than those found by Turolla et al. (2002) by $\Delta\Gamma \sim 1$

One reason for the discrepancy could be that HEROIC assumes isotropic scattering, whereas a correct treatment of the problem should include the anisotropic nature of Thomson scattering[6]. A second likely reason is that bulk Comptonization, being a $(v/c)^2$ effect, is fairly sensitive to how the anisotropic velocity field in the vicinity of a fluid element is treated. The current version of HEROIC uses simple linear interpolation between neighboring cells. We suspect that interpolation will need to be done more carefully before we can reliably model bulk Comptonization.

4 APPLICATIONS TO ACCRETION DISCS

Much of our information on astrophysical black holes comes from observations of their accretion discs. Through modelling the X-ray continuum of accreting stellar-mass black holes in X-ray binaries, it is possible to deduce the structure of the accretion disc. This can then serve as an indirect probe of the physical properties of the black hole (McClintock & Remillard 2006b; McClintock et al. 2014). In the case of supermassive black holes, the vast majority of our information comes from observations of their accretion disc spectra, combined with efforts to model the observations (Krolik 1999a; Koratkar & Blaes 1999).

Spectral modeling of black hole accretion discs is complicated by the fact that the accreting gas is often hot and scattering-dominated. As a result, the emerging radiation from the surface of the disc tends to be significantly "diluted" relative to a blackbody spectrum with the same color temperature. This effect is usually expressed in terms of a color correction factor f defined by

$$T_{\rm col} = f\, T_{\rm eff}, \tag{46}$$

where $T_{\rm col}$ is the color temperature of the emitted radiation and $T_{\rm eff}$ is the effective temperature corresponding to the local disc flux. A key issue then is the estimation of f, since it determines the shape of the resultant disc spectrum. The earliest models typically assumed a constant $f \sim 1.5$ (Mitsuda et al. 1984; Zhang et al. 1997). More recently, much effort has gone towards pinning down f in the case of X-ray binaries (Shimura & Takahara 1995a,b; Merloni et al. 2000; Davis & Hubeny 2006) via sophisticated radiative transfer calculations. In fact, some of the more recent models go beyond a single number f and estimate in detail the complete spectrum of the radiation emerging at each radius of the disc (Davis & Hubeny 2006; Davis et al. 2005, 2006, 2007).

However, all this prior work suffers from a major limitation: it is based on plane parallel atmosphere models. Disc coronae are almost certainly affected strongly by multi-dimensional radiation transfer, and even disc photospheres are expected to be somewhat affected (except perhaps in the geometrically thinnest discs). Monte Carlo methods are very effective for studying multi-dimensional Comptonization in optically thin regions such as the corona (e.g., Davis et al. 2009; Kawashima et al. 2012; Schnittman & Krolik 2013; Schnittman et al. 2013), but they are less useful below the photosphere, where the bulk of the optically thick radiation is generated. This is where we expect HEROIC to be useful, since the code seamlessly straddles the optically thick/thin divide and is inherently multi-dimensional.

Here we present first results from HEROIC. The radiation solutions described below are multi-dimensional, account self-consistently for Comptonization, and include all relativistic effects. The intent here is merely to demonstrate that the code can handle real data taken from GRMHD simulations of discs. More detailed discussion is left to future work.

4.1 Thin Accretion Disc

As a model of a thin accretion disc we use one of the GRMHD thin disc simulations described in Penna et al. (2010), which was run using the code HARM (Gammie et al. 2003; McKinney & Blandford 2009). The simulation did not include radiation but used of an artificial cooling prescription (Shafee et al. 2008; Penna et al. 2010) to keep the disc geometrically thin. From the HARM simulation we obtain the gas density, velocity and viscous heating rate in the accretion disc. We average simulation quantities over time and azimuth and dimensionalize them for a $10M_\odot$ black hole accreting at $\sim 60\%$ Eddington. The latter value is chosen to

[6] Isotropy is built into our formula for the source function, which is written in terms of only the zeroth angular moment J_ν of the radiation. It is relatively straightforward to include higher-order moments like H_ν and K_ν, since these moments are available during the iterations. This will be considered in future upgrades of the code.

be consistent with the vertical thickness $h/r \sim 0.1$ of the simulated model. We also extract an integrated luminosity profile from the GRMHD simulation using the same technique as described in Zhu et al. (2012).

While feeding the simulation data into HEROIC, we rebin the data on a new grid with $n_r = 44$ logarithmically-spaced points in radius, going from $r = 2.17M$ to $r = 50.3M$, and $n_\theta = 64$ points in θ, spaced non-uniformly in such a manner as to preserve the same θ structure as in the original GRMHD grid (i.e., many more points near the equator, where most of the gas is located, than near the poles). The GRMHD data give the vertically integrated energy dissipation rate per unit disc area. To convert this to heating rate per unit volume, we arbitrarily assume that heating is proportional to density,

$$Q^+ \propto \rho, \tag{47}$$

and present results corresponding to this ansatz.[7] For the gas temperature, we initially set $T = 3 \times 10^6$ K in all cells and let HEROIC solve for the temperature.

While running HEROIC, we set both the inner and outer radial grid boundaries to have pure outflow conditions for radiation (i.e., no incident radiation), and the poles to have reflecting boundary conditions (to account for axisymmetry). We use $n_A = 80$ rays in angle and set the frequency resolution to be 10 points per decade over the range $\nu = 10^{16} - 10^{20.5}$ Hz. For the opacities, we assume free-free absorption and Thomson scattering,

$$\alpha_\nu = 1.34 \times 10^{56}\, T^{-1/2} \rho^2 \nu^{-3} (1 - e^{-h\nu/kT})\ \mathrm{cm}^{-1}, \tag{48}$$

$$\sigma_\nu = 0.4\, \rho\ \mathrm{cm}^{-1}, \tag{49}$$

where T is in K, ρ is in $\mathrm{g\,cm}^{-3}$, and ν is in Hz. The models considered here have typically $T \sim 10^7$ K and $\rho \sim 10^{-4} \mathrm{g\,cm}^{-3}$ in the disc interior, so scattering dominates over absorption by a factor of several tens. Hence we expect the escaping radiation to exhibit spectral hardening ($f_{\rm col} > 1$). Also, the vertical optical depth through the disc is quite large, and consequently so is the optical depth across a single cell in the disc interior. Therefore, it is crucial to include ALI (§2.4) while converging to the solution. Typically, we need about 1000 iterations for convergence, though we obtain a fairly good solution already after a few hundred iterations.

Figure 12 shows results obtained with HEROIC for a GRMHD simulation (Penna et al. 2010; Zhu et al. 2012) of a thin accretion disc around a non-spinning black hole ($a_* = 0$). The top left panel shows the heating rate per unit volume versus (r, θ), estimated from the simulation data using equation (47). While running HEROIC, we ignore advection (since this is a thin disc, and also because the simulation data do not provide sufficient information to estimate the level of advection), so we set $Q^- = Q^+$.

The top right panel in Figure 12 shows the distribution of the mean frequency-integrated radiation intensity,

$$J = \int J_\nu d\nu, \tag{50}$$

in the converged solution from HEROIC. The most intense radiation is in the disc interior and has the typical equatorially flattened shape we expect, though the geometrical thickness is not as small as one imagines for a thin disc. Outside the disc is the coronal region where the radiation field is more spherical in shape.

The middle left panel in Figure 12 shows the temperature solution obtained by HEROIC. The disc interior is hotter than the disc surface, as needed to transport out the energy generated in the interior. The spatial variations (streaks) one sees in the interior temperature appear to be driven by non-uniform heating caused by density fluctuations (see eq. 47). The region inside the ISCO ($r < R_{\rm ISCO} = 6M$) contains the hottest gas, distributed almost spherically rather than in a disc. Here the density is low and the gas needs to be hot in order to radiate whatever heating is present. Moreover, advection is not necessarily small (Zhu et al. 2012), though we have chosen to ignore it for the present application. Note that, although the simulation certainly has heating present inside the ISCO (top left panel), in contrast to the predictions of the standard thin disc model (Novikov & Thorne 1973), the amount of heating is not large (see Gammie 1999; Krolik 1999b; Paczyński 2000; Afshordi & Paczyński 2003; Shafee et al. 2008; Noble et al. 2009, 2011; Penna et al. 2010; Kulkarni et al. 2011; Zhu et al. 2012 for conflicting discussions on this issue). Most of the cooling here is by Compton scattering.

Considering next the coronal region above the disc, we see that it is almost isothermal, with T slightly less than 10^7 K. The temperature here is set essentially by the Compton temperature of the escaping radiation, the latter being determined by the emission from the disc combined with hotter radiation coming from the plunging region. There is a small layer of slightly cooler gas just above the disc photosphere. This region is shielded from direct radiation from the plunging region, but does receive scattered radiation from the corona. The cool zone is not as cool as in 1D disc atmosphere models, as we discuss below.

The remaining three panels in Figure 12 show ray-traced images of the converged disc solution as seen by an observer at inclination angle 60 degrees. The middle right panel corresponds to all the radiation emerging from the outer edge of the computational box at $r_{\rm max} = 50M$. The white equatorial band in this panel is off-scale and corresponds to radiation coming out of the disc interior. This should be disregarded since the material here is visible only because we cut the disc at $r = r_{\rm max}$. The lower left panel shows a more realistic view of the disc. Here we have included only those parts of the disc whose the photospheres are located at radii less than $0.9\, r_{\rm max}$. This effectively eliminates the extraneous disc interior regions in the previous panel. The image shows the variation of intensity as a function of radius, with the hottest regions being closest to the center, and there is clear evidence for Doppler boosting of the gas rotating towards the observer (to the left of the black hole) compared to the gas moving away (on the right). The image also shows distortions on the scale of the apparent photon orbit ($r = \sqrt{27}M$), indicated by the white circle. The lower right panel is a closeup which shows the central regions of the image and the "shadow" of the black hole (Bardeen 1973; Luminet 1979; Falcke et al. 2000).

In Figure 13, we compare the disc temperature profile as computed by HEROIC with solutions obtained with the

[7] We also tried models with $Q^+ \propto \rho^2$, ρ^3. As expected, the latter prescriptions put more heating inside the optically thick disc and less in the optically thin corona.

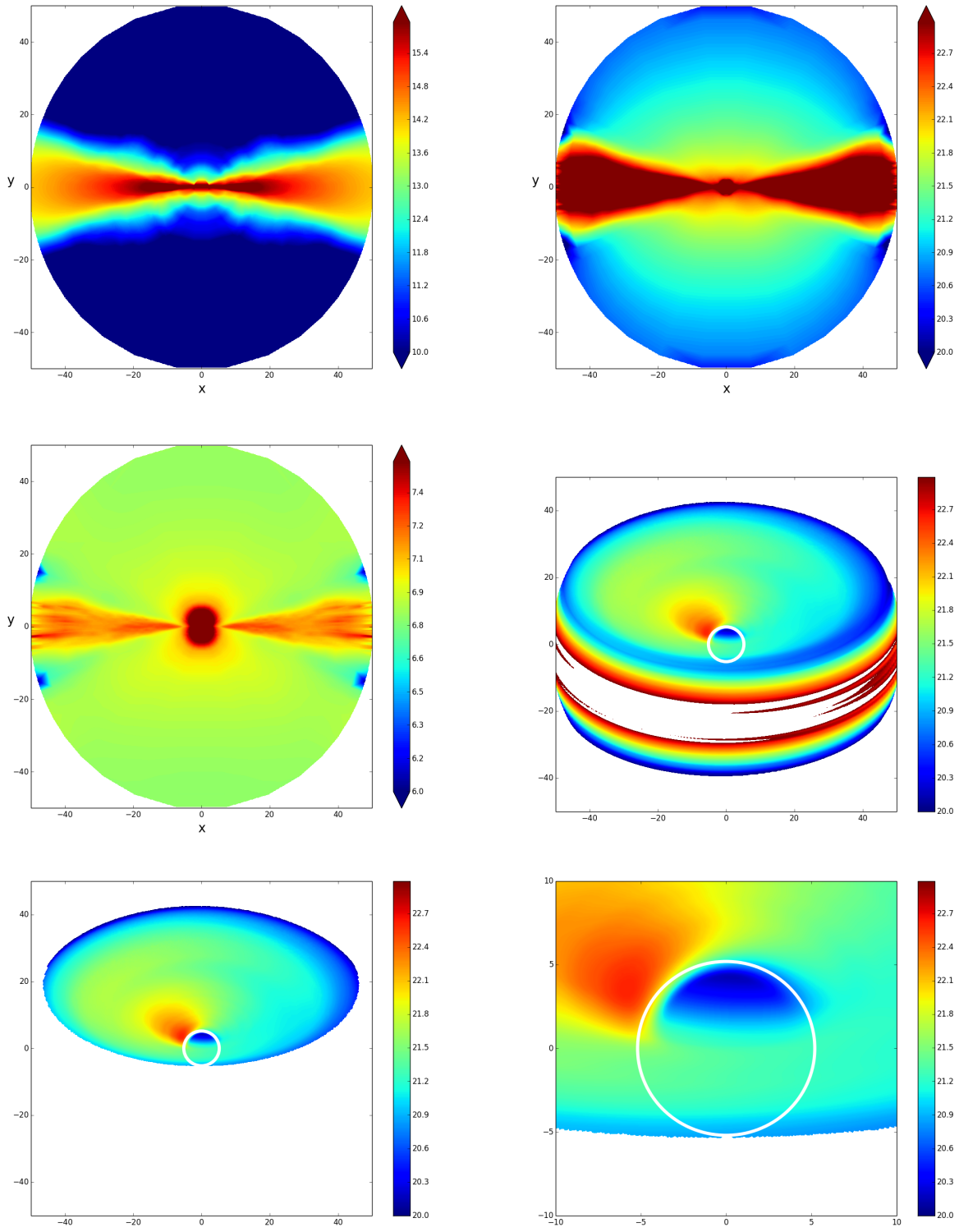

Figure 12. Application of HEROIC to a GRMHD simulation run with HARM of a thin accretion disc around a non-spinning BH. Top Left: Viscous heating rate as a function of position in the poloidal plane, as estimated from the original simulation (see Eq. 47). The BH is located at $x = y = 0$ and the disc mid-plane is oriented horizontally. Top right: Frequency-integrated mean radiation intensity in the converged HEROIC solution. Center left: Gas temperature distribution in the HEROIC solution. Center right: Frequency-integrated ray-traced image of the HEROIC solution for an observer located at an inclination angle of 60 degrees. The white circle corresponds to the apparent size of the photon orbit. Bottom left: Same as the previous panel, but restricted to regions of the solution whose scattering photospheres lie inside $0.9\,r_{\rm max}$. Bottom right: Close-up of the previous panel.

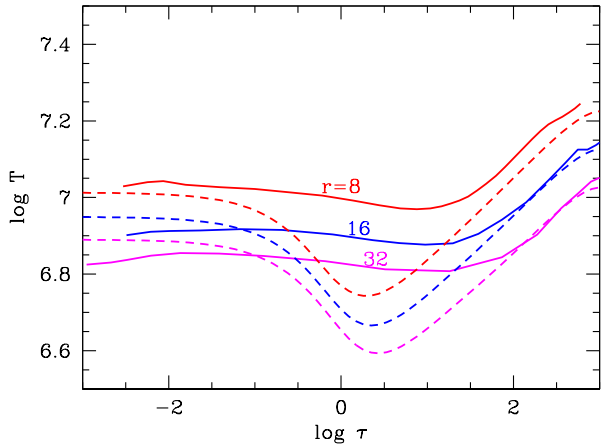

Figure 13. Comparison of HEROIC (solid lines) and TLUSTY (dashed lines) solutions for the vertical temperature profile at $r = 8$ (red), 16 (blue), 32 (magenta), for the thin disc model considered in Figure 12.

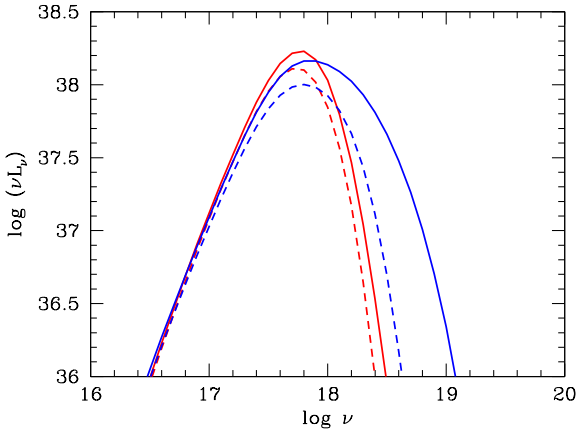

Figure 14. Solid red line: Spectrum as seen by an observer at inclination angle 60 degrees for a GRMHD thin accretion disc around a non-spinning BH (the same model considered in Figures 12 and 13). Dashed red line: Spectrum when the viscous dissipation rate is assumed to be the analytical result from the Novikov & Thorne (1973) model. Blue solid line: Spectrum corresponding to a GRMHD model of a thin disc around a spinning BH with $a_* = 0.9$. Dashed blue line: Spectrum when the heating rate in this model is set equal to the prediction of thin disc theory.

1D radiative transfer code TLUSTY.[8] In both models, the temperature profile inside the optically thick disc interior takes on a characteristic $T \propto \tau^{1/4}$ form, where τ is the optical depth from the disc surface. The primary difference between TLUSTY and HEROIC occurs above the disc's effective photosphere. The temperature profile in HEROIC tends towards isothermality whereas the TLUSTY solution has a pronounced temperature dip at the surface. This difference is partly due to the 3D propagation of radiation, specifically, the effect of gravitationally lensed returning radiation from the disc and scattered radiation from the corona. The incoming flux can penetrate downwards through the cool photospheric surface and drive the gas towards isothermality via Compton heating. Some differences between the 3D GRMHD result and the 1D TLUSTY calculation are also due to differences in the mass distribution within the disc. TLUSTY computes the vertical structure of the disc via the condition of hydrostatic equilibrium, but accounting only for gas and radiation pressure. HEROIC does not solve for the vertical density structure, but takes it from the GRMHD simulation. In the latter, there is substantial magnetic pressure support and this tends to puff up the disc, producing structures with more mass at larger height.

The very large difference between the HEROIC and TLUSTY temperature profiles near the disc photosphere is likely to have observational consequences. For instance, models of AGN spectra based on plane parallel atmospheres have a difficult time explaining the absence of Lyman and other edges in observed spectra (Koratkar & Blaes 1999). The flat temperature profile with depth predicted by HEROIC might provide an explanation (Shane Davis, private communication).

Figure 14 shows spectra as seen by an observer at an inclination angle of 60 degrees for two models: (i) the GRMHD simulation with a non-spinning BH discussed so far (red lines), and (ii) an equivalent simulation for a spinning BH with $a_* = a/M = 0.9$ (Zhu et al. 2012) (blue lines). These spectra are computed using the ray-tracing code for an observation plane located at $r = 10^5$. Starting with the non-spinning BH model, the solid red line corresponds to the model discussed previously, while the dashed red line corresponds to a model in which Q^+ is set equal to the analytical prediction of the Novikov & Thorne (1973) model for the same accretion rate. The latter has no viscous heating inside the ISCO, whereas the former does (the heating rates outside the ISCO are also modestly different because of non-zero stress at the ISCO). The GRMHD model thus predicts a larger luminosity than the equivalent Novikov & Thorne (1973) model (see Penna et al. 2010; Kulkarni et al. 2011; Noble et al. 2011; Zhu et al. 2012). However, the shape of the spectrum is very similar, suggesting that efforts to measure BH spin by fitting the continuum spectrum of the disc are likely to be reasonably accurate (McClintock et al. 2014). The spectra corresponding to the spin 0.9 GRMHD simulation (blue lines) are noticeable hotter for a comparable luminosity, as expected from thin disc theory, and this again validates efforts to measure BH spin using disc continuum spectra. However, here the solid and dashed lines differ more substantially. The extra dissipation at small radii in the GRMHD simulation causes the hot gas here to radiate a fair bit, leading to significantly more emission at high frequencies.

[8] The TLUSTY solution assumes that disc heating is proportional to the density, which is the same as in the HEROIC solution presented here.

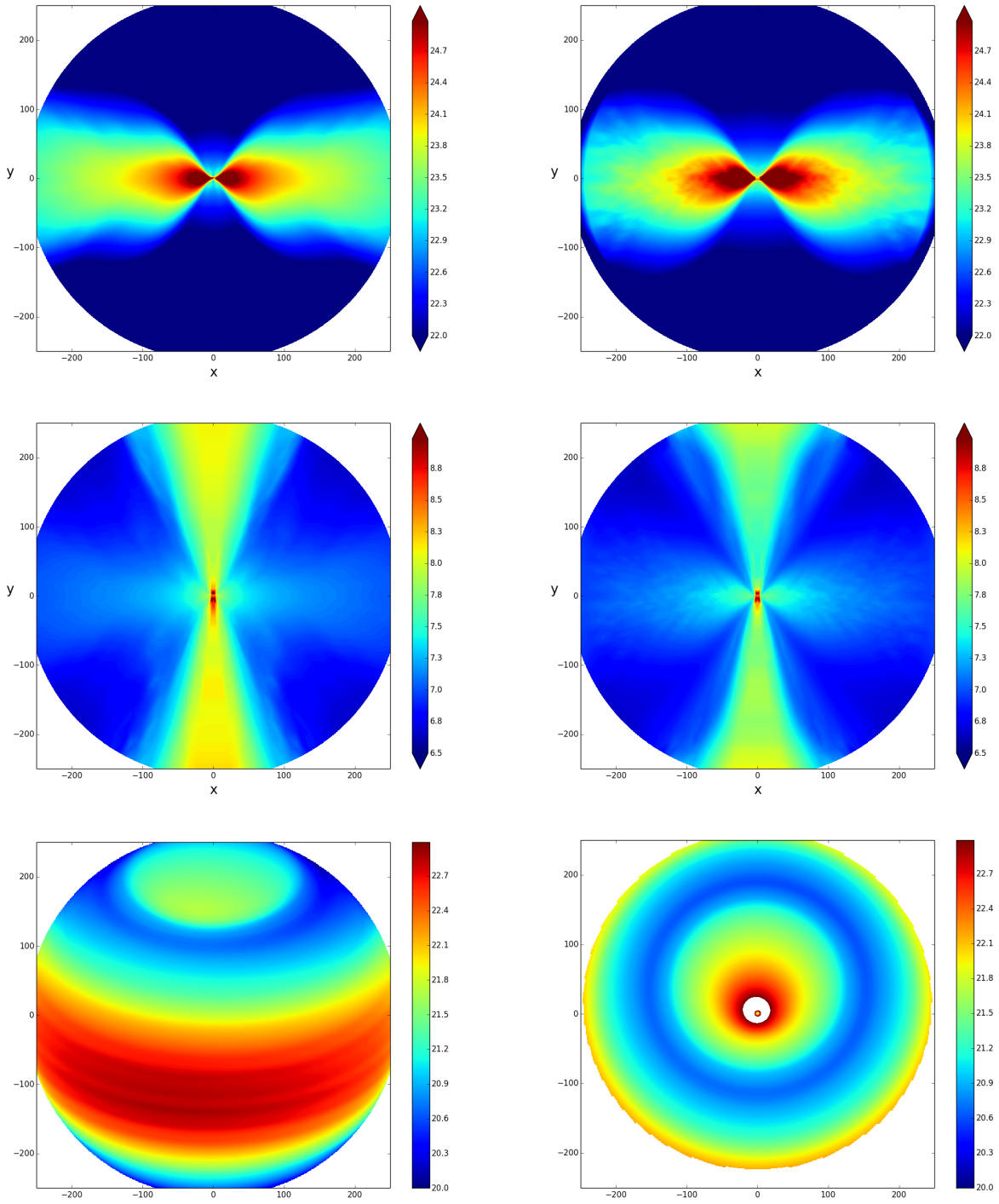

Figure 15. Application of HEROIC to a GRRMHD simulation run with KORAL of a super-Eddington ($\dot{m} = 11$) accretion disc around a non-spinning BH. The BH is located at $x = y = 0$ and the disc mid-plane is oriented horizontally. Top left: Frequency-integrated mean intensity of the radiation field in the fluid frame as obtained from KORAL. Top right: Same quantity as determined from the converged HEROIC solution. Center left: Gas temperature distribution from KORAL. Center right: Gas temperature distribution in the converged HEROIC solution. Bottom left: Frequency-integrated ray-traced image of the HEROIC solution for an observer located at an inclination angle of 60 degrees. Bottom right: Image for an observer at 10 degrees, but showing only the regions of the solution at $\theta < 70$ degrees.

4.2 Supercritical Accretion Disc

For our second application we consider a general relativistic radiation MHD (GRRMHD) simulation of a supercritical ($\dot{m} > \dot{m}_{\rm Edd}$) accretion flow run with the code KORAL (Sądowski et al. 2013, 2014). The particular simulation we analyse is taken from Sądowski & Narayan (2015) and corresponds to a $10M_\odot$ BH accreting at about 11 times the Eddington rate. This simulation used a photon-conserving form of Comptonization. From the time-averaged simulation data we obtain the density and four-velocity of the fluid. These quantities are input into HEROIC on a grid going from $r = 3.4$ to $r = 250$. Since KORAL evolves the radiation field, it obtains directly the cooling rate Q^- as a function of position. From this, we calculate Q^+ via equation (39); in this step, we use the KORAL temperature for consistency. However, once we input these Q^+ values into HEROIC and as the iterations proceed, we use the HEROIC-derived temperatures to estimate Q^-, again through equation (39). HEROIC is run with 80 ray angles and 61 frequencies distributed uniformly in $\log\nu$ between $\nu = 10^{16}$ Hz and $\nu = 10^{22}$ Hz. For the opacities we use equations (48) and (49).

Figure 15 shows the results. The top left panel shows the mean intensity J (see eq. 50) obtained in the KORAL simulation. Since this is a super-Eddington flow, the optically thick regions of the disc are geometrically thick. Along the poles are two moderately wide funnels which are optically thin. Radiation from the main disc flows into the funnel and escapes in twin beams, while at the same time accelerating polar gas in relativistic jets. Note that the very central region of the funnel is somewhat devoid of radiation (the tiny thin vertical drak blue line at the axis). This is a well-known weakness of the M1 closure scheme on which KORAL is based (Sądowski et al. 2014), although the effect is not as strong as it could be in this particular simulation since an artificial radiation viscosity was applied (Sądowski et al. 2015). The top right panel in Figure 15 shows the mean radiation intensity obtained by HEROIC for the same system. The solution is very similar to the KORAL solution in the main disc. The funnel region, however, is smoother than in the previous panel. In particular, the radiation deficit near the pole is no longer present. Also, the HEROIC radiation field is a little stronger compared to KORAL in the funnel.

The middle two panels in Figure 15 show the temperature distributions obtained with KORAL (left) and HEROIC (right). There are some differences in the disc interior, but these are not important since they do not affect the radiation that reaches the observer. For the latter, what matters is the temperature in the optically thin funnel region and at the photosphere. Here we see fairly good agreement, though HEROIC gives slightly lower temperatures than KORAL. A likely reason for this is the fact that the radiation density is different in the two models, as already discussed. Since the gas temperature in the funnel is largely determined by Compton scattering, it is natural for the HEROIC model with its larger radiation energy density to be cooler. It should also be kept in mind that KORAL uses a crude representation of the radiation, which consists of just the bolometric energy density and bolometric flux (4 numbers at each location), and computes the radiative transport with frequency-integrated effective opacities. The HEROIC model shown here, by contrast, solves for the intensities on 80 ray angles, each over 61 frequencies, and uses a frequency-dependent opacity (eq. 48). These are large differences, and it is natural for the results to deviate.

The bottom panels in Figure 15 show ray-traced images. The panel on the left shows all the radiation from the HEROIC solution as would be seen by an observer at an inclination angle of 60 degrees. This is not particularly meaningful because most of the gas is optically very thick and even the optically thin region in the funnel at the top would not be visible if we had not truncated the model at $r_{\rm max} = 250$. Nevertheless, the similarity to the bottom left panel in Figure 9 of Ohsuga et al. (2005) is striking, despite the many differences in the methods used in the two studies. The right panel in Figure 15 shows the view of the region of the solution at $\theta < 70$ degrees for an observer at a low inclination angle of 10 degrees. This observer, and others up to an inclination angle of around 25 degrees, will be able to see the walls of the funnel (the circular central cyan-green-yellow-red region) and down near the BH horizon (maroon-white). In the image of a real system, this funnel region would be surrounded by the photosphere of the rest of the optically thick disc. However, the KORAL simulation under consideration did not extend over a large enough volume to reliably model the photosphere. Therefore, the outer half of the image shown in this panel (starting with dark blue, extending to cyan-green-yellow) should not be taken too seriously.

The upper panel in Figure 16 shows spectra of radiation emerging from the funnel as viewed by observers at various inclination angles. Here, the funnel is defined as any region for which the scattering photosphere lies below $0.9\,r_{\rm max}$. The three red spectra at the top correspond to pole-on observers who are able to see all the way down to the BH. For these observers, the object would appear as a bright super-Eddington X-ray source with peak emission at around 5 keV. The remaining blue spectra are for more inclined observers. However, these spectra are less meaningful since radiation from the funnel escapes in these directions only because we trucated the disc at $r_{\rm max}$. In a real system, the funnel would extend farther out in radius and no radiation from the hot inner regions would go towards the sides.

The spectra in the upper panel in Figure 16 are too peaked and blackbody-like compared to the spectra obtained by Kawashima et al. (2012) from analogous Newtonian radiation-hydrodynamic simulations of super-Eddington accretion discs. In part this is because they considered also radiation from the more optically thick wind outside the funnel. Therefore, for comparison, we show in the lower panel of Figure 16 spectra as seen by distant observers but now considering the entire HEROIC solution out to polar angle $\theta = 70\,$deg. These spectra do have more radiation at softer photon energies and more closely resemble the results shown in Kawashima et al. (2012). However, the HEROIC spectra are a little too soft, peaking at about 5 keV rather than at 10 keV.

Finally, Figure 17 shows several versions of the istropic equivalent luminosity $L_{\rm iso}$ of the supercritical BH accretion model under consideration as a function of inclination angle. The various lines are obtained by taking the radial flux as a function of θ at the outer edge of the box ($r_{\rm max} = 250$) and converting it to an effective isotropic equivalent lumi-

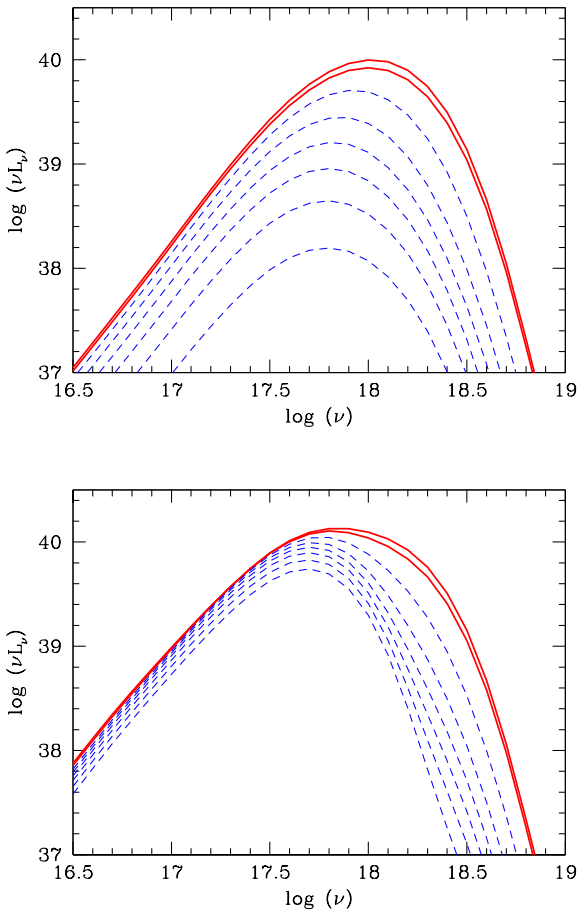

Figure 16. Top panel: Spectra corresponding to radiation from the funnel region of the super-Eddington BH accretion model considered in Fig. 15. Solid red lines: Spectra as seen by observers at inclination angle (from above) 10 and 20 degrees, respectively. Dashed blue lines: Spectra for observers at (from above) 30, 40, 50, 60, 70, 80 degrees, respectively. Lower panel: Spectra when the entire region of the model up to $\theta = 70$ deg is considered.

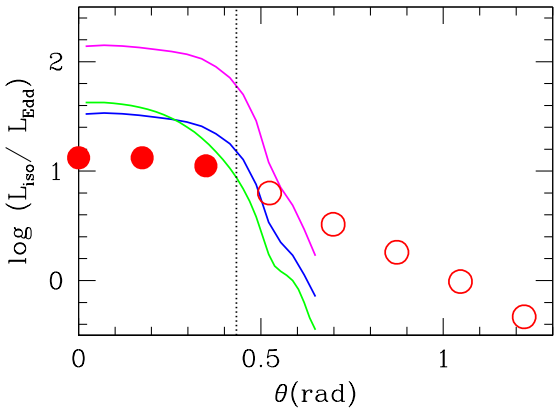

Figure 17. Isotropic equivalent luminosity (in Eddington units) of the super-Eddington BH accretion model considered in Figures 15 and 16, as a function of polar angle θ. Green line: Luminosity estimated from the original KORAL simulation based on the radial radiative flux at the outer edge of the box, $r = r_{\rm max} = 250$. Magenta line: Luminosity estimated at the same radius from the HEROIC solution when the gas temperature is held fixed at the KORAL values. Blue line: Luminosity from the HEROIC solution when the temperature is solved self-consistently within HEROIC. Vertical dotted line: Nominal edge of the optically thin funnel region. Red symbols: Isotropic equivalent luminosity measured by a distant observer as a function of inclination angle. Only radiation emerging from inside the funnel region is included. Solid symbols are more meaningful since the BH at the base of the funnel is visible to these observers.

nosity. The green line shows the luminosity from the original KORAL simulation. Here, the funnel region corresponds to $\theta < 0.43$ rad, indicated by the vertical dotted line. This is the only part of the radiation that is guaranteed to escape to infinity. The radiation at larger angles is inside optically thick gas (even at $r = 250$) and it is not clear what fraction of this energy flux will finally escape as radiation.

The magenta line in Figure 17 shows the isotropic equivalent luminosity at $r = 250$ obtained from the HEROIC solution when we keep the gas temperature fixed at the KORAL values and solve self-consistently only for the radiation field. This curve has qualitatively the correct shape versus θ, but the luminosity is several times too large. On the other hand, the blue line shows the result when we solve for both the temperature and the radiation field with HEROIC (all the previous results in Figs. 16 and 15 correspond to this solution). Now we see much closer agreement with the KORAL result. The HEROIC profile is slightly more flat-topped, but the integrated luminosity is close. This comparison highlights the important point that, when post-processing GRRMHD simulations, it is necessary to solve self-consistently for the gas temperature, a point made earlier by Schnittman et al. (2013). It is particularly important with Comptonization because small changes in the temperature can cause large changes in the radiation energy density.

The red symbols in Figure 17 show the isotropic equivalent luminosity as measured by distant observers located at different inclination angles. These are computed from the HEROIC model corresponding to the blue line, i.e., with both temperature and radiation field calculated self-consistently. Only the results corresponding to small inclination angles (< 25 deg, shown by solid symbols) are meaningful. For these observers, the apparent luminosity will be highly super-Eddington. In fact, both the luminosity and the spectrum (Fig. 16) for these face-on observers agree qualitatively with observations of ultra-luminous X-ray sources (e.g., Miyawaki et al. 2009; Kawashima et al. 2012). Note that, on top of the luminosities computed here, there would be an additional $\sim 1 L_{\rm Edd}$ of radiation from the rest of the optically thick disc. This is a small correction, but it would have a softer spectrum and would make noticeable changes to the low-energy end of the spectra shown in Figure 16.

A notable feature of the red symbols in Figure 17 is that, at small angles, they lie below the blue line by a factor > 2. That is, if we estimate the luminosity at a given

θ in the funnel via the radiative flux at radius $r_{\rm max}$ (blue line), the result will be an overestimate compared to the luminosity that an observer at infinity at the same inclination angle θ would observe (filled red circle). This is just a matter of geometry. A good fraction of the radiation at $r_{\rm max}$ goes off sideways towards observers at larger inclination angles, which is why the open circles in Figure 17 lie above the corresponding blue line. One other relevant comment is that HEROIC assumes a thermal medium, whereas some of the emission from the jet in the funnel might be non-thermal. Such a component would appear as a high energy power-law tail in the spectrum.

5 SUMMARY AND DISCUSSION

In this paper we described an extension of our radiative transfer code HERO (Paper 1) that now enables us to handle Compton scattering. Given the density, velocity and heating rate of the gas as a function of position, the new code HEROIC self-consistently solves for both the radiation field and the gas temperature. The code handles a wide range of optical depths, from optically very thick to very thin, and operates in multiple dimensions within a general relativistic space-time. It is suitable for modeling radiation in high energy astrophysical objects where thermal Comptonization is important.

We described a number of tests of HEROIC. We showed that the code reproduces known results for thermal Comptonization, both in one dimension (plane parallel geometry) and in multiple dimensions (spherical geometry treated in axisymmetry). It also handles relativistic effects like Doppler shift, which is important for modeling radiation trapping and advection, gravitational redshift, and ray-deflection. In addition, the code produces bulk Comptonization when there is a converging flow (as in spherical accretion), though the slope of the power-law tail is too soft.

The inability of HEROIC to model bulk Comptonization accurately is likely because the code assumes isotropic scattering rather than using the correct angular distribution. This could be rectified in the future. Also, only a short characteristics version of HEROIC is available at the moment; the next step is to develop a long characteristics version. Neither of these shortcomings is serious, and both are easily overcome. A more important limitation is that HEROIC assumes the gas to be thermal and in LTE. Extension to NLTE is possible, in principle, but will require a major upgrade. Extension to non-thermal processes would be equally difficult, requiring at the very least prescriptions for the energy-dependent heating of non-thermal electrons and for various opacities.

Other limitations are inherent to the very structure of HEROIC and cannot be overcome. The code assumes that there is no time dependence in any quantity, thus it is most appropriate for studying time-averged properties of objects. HEROIC could be used to study time-dependent phenomena, but it would have to be under the "fast-light" approximation, where time delays are not taken into account. HEROIC is a *radiation post-processor* which takes density, velocity, etc. from other codes and obtains a more detailed, and hopefully more accurate, solution for the radiation field. In the process it also improves the gas thermodynamics by re-solving for the temperature. However, there is no dynamics in the code. In principle, for simple geometries, e.g., plane parallel or spherically symmetric systems, dynamics could be built into the structure of the code by including additional conditions (force equation, energy equation), but it is not clear that this would be an improvement on other simpler codes.

As examples of how HEROIC might be used, we presented in this paper two applications. First, we took a GRMHD simulation of a thin accretion disc around a BH and used HEROIC to solve for the gas temperature and radiation field. The original GRMHD simulation did not include radiation but used an artificial cooling prescription. Therefore, we had to make an educated guess regarding the distribution of viscous heating in the system. Given this guess, HEROIC was successfully able to solve the multi-dimensional radiative transfer problem. The most striking result was that the temperature profile determined by HEROIC was noticeably different from that previously obtained from 1D plane-parallel disc atmosphere models. This effect could have implications for modeling disc spectra and deserves to be studied further.

In the second application, we took data from a GRRMHD simulation of a supercritical accretion disc around a BH (accretion rate of 11 Eddington) and solved for the gas temperature and radiation field using HEROIC. We confirmed that observers who view such a system from small inclination angles would see very large apparent luminosities, up to tens of Eddington. The spectrum could still be quite thermal (assuming there is no non-thermal heating of electrons) and blackbody-like, and there might not be any spectral indication for relativistic beaming. Models like this may explain apparently super-Eddington objects such as ultra-luminous X-ray sources.

To conclude, we view HEROIC as a tool to bridge the gap between GRMHD/GRRMHD simulations and observations. The simulations that have been done to date are highly sophisticated in their treatment of dynamics, but they are relatively crude in how they handle radiation. Either they ignore radiation altogether (GRMHD) or, as in the GRRMHD codes currently available for simulating black hole accretion (Sądowski et al. 2014; McKinney et al. 2014; Fragile et al. 2014; Takahashi & Ohsuga 2015), they treat radiation effectively as a fluid described by a few angular moments. More sophisticated techniques have been applied to treat radiation in Newtonian simulations of discs (Jiang et al. 2012, 2014), but even these methods, while allowing more angular structure in the radiation field, are generally limited to frequency-integrated quantities. It is far too expensive to run multi-dimensional hydrodynamic or MHD simulations and to follow at the same time at each spatial location many ray directions and many frequencies. Until computers become much more powerful than they are today, post-processing of simulation output seems to be the only way. HEROIC is designed to fill this need.

6 ACKNOWLEDGEMENTS

RN and YZ were supported in part by NSF grant AST1312651. RN also received partial support under NASA grant TCAN NNX14AB47G. AS acknowledges support by

NASA through Einstein Postdoctotral Fellowship number PF4-150126 awarded by the Chandra X-ray Center, which is operated by the Smithsonian Astrophysical Observatory for NASA under contract NAS8-03060. AS also thanks the Harvard-Smithsonian Center for Astrophysics for hospitality. The authors acknowledge computational support from NSF via XSEDE resources (grant TG-AST080026N), and from NASA via the High-End Computing (HEC) Program through the NASA Advanced Supercomputing (NAS) Division at Ames Research Center.

APPENDIX A: THE FOKKER-PLANCK EQUATION FOR COMPTONIZATION

In the limit of small changes in the photon energy per scattering, Comptonization of an isotropic distribution of photons is described by the Fokker-Planck equation (Barbosa 1982)

$$\frac{\partial n}{\partial t} = \frac{1}{\nu^2}\frac{\partial}{\partial \nu}\left\{ n(1+n)\left[-\nu^2\left\langle\frac{\Delta\nu}{\tau}\right\rangle + \frac{\partial}{\partial\nu}\left(\nu^2\left\langle\frac{(\Delta\nu)^2}{2\tau}\right\rangle\right)\right] + \nu^2\left\langle\frac{(\Delta\nu)^2}{2\tau}\right\rangle\frac{\partial n}{\partial\nu}\right\}, \tag{A1}$$

where $n(\nu,t)$ is the photon distribution function, $\langle\Delta\nu/\tau\rangle$ is the mean change in the photon frequency ν per scattering, $\langle(\Delta\nu)^2/2\tau\rangle$ is the mean dispersion per scattering, and τ is the scattering optical depth per unit time.

We rewrite this equation in a more familiar notation by defining

$$t_c = (n_e\sigma_T c)t = \frac{t}{\tau}, \tag{A2}$$

$$x = \frac{h\nu}{kT} = \frac{\epsilon}{kT}, \tag{A3}$$

where ϵ is the photon energy. We also define

$$\left\langle\frac{\Delta\nu}{\nu}\right\rangle = \left\langle\frac{\Delta\epsilon}{\epsilon}\right\rangle = \xi, \tag{A4}$$

$$\left\langle\frac{(\Delta\nu)^2}{2\nu^2}\right\rangle = \left\langle\frac{(\Delta\epsilon)^2}{2\epsilon^2}\right\rangle = \zeta, \tag{A5}$$

where $\epsilon = h\nu$ is the photon energy. Then, equation (A1) becomes

$$\frac{\partial n}{\partial t_c} = \frac{1}{x^2}\frac{\partial}{\partial x}\left[\zeta x^4\frac{\partial n}{\partial x} + \left\{\frac{\partial}{\partial x}\left(\zeta x^4\right) - \xi x^3\right\} n(n+1)\right]. \tag{A6}$$

If we substitute in this equation the standard low-temperature, low-frequency expressions, viz., $\xi = (kT/mc^2)(4-x) \equiv \theta_e(4-x)$, and $\zeta = \theta_e$, we recover the Kompaneets equation

$$\frac{\partial n}{\partial t_c} = \theta_e\frac{1}{x^2}\frac{\partial}{\partial x}\left[x^4\left\{\frac{\partial n}{\partial x} + n(n+1)\right\}\right]. \tag{A7}$$

In many settings in high-energy astrophysics, the electron temperature is comparable to or even higher than the electron rest mass. In order to calculate the effects of Compton scattering in such settings, we would need to include a large number of higher-order terms in the Fokker-Planck equation (A1) or, even better, employ the full scattering integral of Comptonization (see, e.g., Suleimanov et al. 2012). Such an approach, however, would be very expensive computationally and would severely impact our ability to run long simulations of accretion flows. Instead, we use an approximate method to calculate the effects of Comptonization in high-temperature flows, which we describe below.

In the limit of high electron temperatures, when a mono-energetic ensemble of soft photons is scattered by a relativistic distribution of electrons, the energy distribution of the scattered photons can be approximated by a log-normal distribution (see, e.g., Figure 12 of Pozdnyakov et al. 1983). This can be understood given the fact that the energy of each photon exponentially increases after each scattering, i.e.,

$$\epsilon' = \epsilon\, e^y\,, \tag{A8}$$

where ϵ and ϵ' are the photon energies before and after scattering and y is a variable whose distribution has a mean of ξ and a dispersion of 2ζ. In the limit of very small energy change per scattering, i.e., when $y \ll 1$, equation (A8) reduces to $\epsilon' = \epsilon(1+y)$ and the definitions of ξ and ζ become identical to those in equations (A4)–(A5). If we approximate the distribution over the values of y by a normal distribution

$$P(y)dy \propto \exp\left[-\frac{(y-\xi)^2}{2(2\zeta)}\right], \tag{A9}$$

then we can write for the distribution over the energies of the scattered photons

$$I(\epsilon) = P(y)\left|\frac{d\epsilon}{dy}\right|^{-1} \tag{A10}$$

or, equivalently,

$$\epsilon I(\epsilon) \propto \exp\left[-\frac{\ln(\epsilon/\epsilon_{\rm max})^2}{4\zeta}\right], \tag{A11}$$

where $\epsilon_{\rm max} = \epsilon\, e^{\xi}$ is the most likely value for the energy.

Under this approximation, we can now use the same Fokker-Planck form for the evolution of the photon distribution function, but with this more general definition for ξ and ζ. Effectively, we are integrating out all the higher-order terms in the expansion of the Fokker-Planck equation, incorporating their effects by modifying the functional forms of ξ and ζ. In obtaining these modifications, we are guided by the fact that the photon distribution function has certain well-defined properties. In particular, as $t_c \to \infty$, the photon distribution function has to settle down to a Bose-Einstein distribution,

$$n(x) = \frac{1}{Ce^x - 1}, \tag{A12}$$

which automatically satisfies

$$\frac{\partial n}{\partial x} = -n(n+1). \tag{A13}$$

Furthermore, in the limit $t_c \to \infty$, the quantity inside the square brackets [...] in equation (A6), which represents the flux of photons along the energy coordinate x, has to vanish (thermodynamic equilibrium). Therefore, we have the strong requirement that

$$\frac{\partial}{\partial x}(\zeta x^4) - \zeta x^4 - \xi x^3 = 0\,. \tag{A14}$$

Inserting this into equation (A6), we obtain

$$\frac{\partial n}{\partial t_c} = \frac{1}{x^2}\frac{\partial}{\partial x}\left\{\zeta x^4\left[\frac{\partial n}{\partial x} + n(n+1)\right]\right\}. \tag{A15}$$

In the limit of very small photon energy before scattering, ζ becomes independent of x (see Barbosa 1982) and, therefore, the condition (A14) reduces to $\xi = \zeta(4-x)$ and the Fokker-Planck equation becomes

$$\frac{\partial n}{\partial t_c} = \frac{1}{x^2}\frac{\partial}{\partial x}\left\{\zeta x^4\left[\frac{\partial n}{\partial x} + n(n+1)\right]\right\}. \quad \text{(A16)}$$

In (Sądowski & Narayan 2015) we used the approximate relation

$$\xi = \frac{(1+3.683\theta_e+4\theta_e^2)}{(1+\theta_e)}\,\theta_e(4-x), \quad \text{(A17)}$$

derived to fit the high temperature behavior of the scattering process (when $\epsilon \ll kT$), which obeys the requirement that $\xi/(4-x)$ must be independent of x. Incorporating this expression into the Fokker-Planck equation, we obtain

$$\frac{\partial n}{\partial t_c} = \frac{(1+3.683\theta_e+4\theta_e^2)}{(1+\theta_e)}\,\theta_e \frac{1}{x^2}\frac{\partial}{\partial x}\left\{x^4\left[\frac{\partial n}{\partial x} + n(n+1)\right]\right\}. \quad \text{(A18)}$$

REFERENCES

Afshordi N., Paczyński B., 2003, ApJ, 592, 354
Barbosa D. D., 1982, ApJ, 254, 301
Bardeen J. M., 1973, in Dewitt C., Dewitt B. S., eds, Black Holes (Les Astres Occlus) Timelike and null geodesics in the Kerr metric.. pp 215–239
Becker P. A., 2003, MNRAS, 343, 215
Begelman M. C., 1979, MNRAS, 187, 237
Broderick A., Blandford R., 2003, MNRAS, 342, 1280
Chang J. S., Cooper G., 1970, Journal of Computational Physics, 6, 1
Coppi P. S., Blandford R. D., 1990, MNRAS, 245, 453
Davis S. W., Blaes O. M., Hirose S., Krolik J. H., 2009, ApJ, 703, 569
Davis S. W., Blaes O. M., Hubeny I., Turner N. J., 2005, ApJ, 621, 372
Davis S. W., Done C., Blaes O. M., 2006, ApJ, 647, 525
Davis S. W., Hubeny I., 2006, ApJS, 164, 530
Davis S. W., Woo J.-H., Blaes O. M., 2007, ApJ, 668, 682
Dexter J., Agol E., 2009, ApJ, 696, 1616
Dolence J. C., Gammie C. F., Mościbrodzka M., Leung P. K., 2009, ApJS, 184, 387
Done C., Gierliński M., Kubota A., 2007, A&A Rev., 15, 1
Dovčiak M., Karas V., Yaqoob T., 2004, ApJS, 153, 205
Falcke H., Melia F., Agol E., 2000, ApJL, 528, L13
Fragile P. C., Olejar A., Anninos P., 2014, ApJ, 796, 22
Gammie C. F., 1999, ApJL, 522, L57
Gammie C. F., McKinney J. C., Tóth G., 2003, ApJ, 589, 444
Gierlinski M., Zdziarski A. A., Done C., Johnson W. N., Ebisawa K., Ueda Y., Haardt F., Phlips B. F., 1997, MNRAS, 288, 958
Gorecki A., Wilczewski W., 1984, Acta Astron., 34, 141
Grove J. E., Johnson W. N., Kroeger R. A., McNaron-Brown K., Skibo J. G., Phlips B. F., 1998, ApJ, 500, 899
Haardt F., 1993, ApJ, 413, 680
Haardt F., Maraschi L., 1991, ApJL, 380, L51
Hubeny I., 2003, in Hubeny I., Mihalas D., Werner K., eds, Stellar Atmosphere Modeling Vol. 288 of Astronomical Society of the Pacific Conference Series, Accelerated Lambda Iteration: An Overview. p. 17
Hubeny I., Blaes O., Krolik J. H., Agol E., 2001, ApJ, 559, 680
Jiang Y.-F., Stone J. M., Davis S. W., 2012, ApJS, 199, 14
Jiang Y.-F., Stone J. M., Davis S. W., 2014, ApJ, 796, 106
Joss P. C., 1977, Nature, 270, 310
Kawashima T., Ohsuga K., Mineshige S., Yoshida T., Heinzeller D., Matsumoto R., 2012, ApJ, 752, 18
Kojima Y., 1991, MNRAS, 250, 629
Koratkar A., Blaes O., 1999, PASP, 111, 1
Krolik J. H., 1999a, Active galactic nuclei : from the central black hole to the galactic environment
Krolik J. H., 1999b, ApJL, 515, L73
Kulkarni A. K., Penna R. F., Shcherbakov R. V., Steiner J. F., Narayan R., Sä Dowski A., Zhu Y., McClintock J. E., Davis S. W., McKinney J. C., 2011, MNRAS, 414, 1183
Laor A., Netzer H., Piran T., 1990, MNRAS, 242, 560
Luminet J.-P., 1979, A&A, 75, 228
Madej J., 1989, ApJ, 339, 386
McClintock J. E., Narayan R., Steiner J. F., 2014, Space Sci. Rev., 183, 295
McClintock J. E., Remillard R. A., 2006a, Black hole binaries. pp 157–213
McClintock J. E., Remillard R. A., 2006b, Black hole binaries. pp 157–213
McKinney J. C., Blandford R. D., 2009, MNRAS, 394, L126
McKinney J. C., Tchekhovskoy A., Sądowski A., Narayan R., 2014, MNRAS, 441, 3177
Merloni A., Fabian A. C., Ross R. R., 2000, MNRAS, 313, 193
Mihalas D., 1978, Stellar atmospheres /2nd edition/
Mitsuda K., Inoue H., Koyama K., Makishima K., Matsuoka M., Ogawara Y., Suzuki K., Tanaka Y., Shibazaki N., Hirano T., 1984, PASJ, 36, 741
Miyawaki R., Makishima K., Yamada S., Gandhi P., Mizuno T., Kubota A., Tsuru T. G., Matsumoto H., 2009, PASJ, 61, 263
Mościbrodzka M., Falcke H., Shiokawa H., Gammie C. F., 2014, A&A, 570, A7
Noble S. C., Krolik J. H., Hawley J. F., 2009, ApJ, 692, 411
Noble S. C., Krolik J. H., Schnittman J. D., Hawley J. F., 2011, ApJ, 743, 115
Novikov I. D., Thorne K. S., 1973, in Dewitt C., Dewitt B. S., eds, Black Holes (Les Astres Occlus) Astrophysics of black holes.. pp 343–450
Ohsuga K., Mori M., Nakamoto T., Mineshige S., 2005, ApJ, 628, 368
Paczyński B., 2000, ArXiv Astrophysics e-prints
Penna R. F., McKinney J. C., Narayan R., Tchekhovskoy A., Shafee R., McClintock J. E., 2010, MNRAS, 408, 752
Pomraning G. C., 1973, The equations of radiation hydrodynamics
Ponman T. J., Foster A. J., Ross R. R., 1990, MNRAS, 246, 287
Poutanen J., Svensson R., 1996, ApJ, 470, 249
Pozdnyakov L. A., Sobol I. M., Syunyaev R. A., 1983, Astrophysics and Space Physics Reviews, 2, 189

Press W. H., Teukolsky S. A., Vetterling W. T., Flannery B. P., 1992, Numerical recipes in FORTRAN. The art of scientific computing
Prokhorov D. A., Antonuccio-Delogu V., Silk J., 2010, A&A, 520, A106
Psaltis D., 2001, ApJ, 555, 786
Psaltis D., Johannsen T., 2012, ApJ, 745, 1
Rauch K. P., Blandford R. D., 1994, ApJ, 421, 46
Reynolds C. S., 2014, Space Sci. Rev., 183, 277
Rybicki G. B., Lightman A. P., 1979, Radiative processes in astrophysics
Sądowski A., Narayan R., 2015, ArXiv e-prints
Sądowski A., Narayan R., McKinney J. C., Tchekhovskoy A., 2014, MNRAS, 439, 503
Sądowski A., Narayan R., Tchekhovskoy A., Abarca D., Zhu Y., McKinney J. C., 2015, MNRAS, 447, 49
Sądowski A., Narayan R., Tchekhovskoy A., Zhu Y., 2013, MNRAS, 429, 3533
Schnittman J. D., Krolik J. H., 2013, ApJ, 777, 11
Schnittman J. D., Krolik J. H., Noble S. C., 2013, ApJ, 769, 156
Shafee R., McKinney J. C., Narayan R., Tchekhovskoy A., Gammie C. F., McClintock J. E., 2008, ApJL
Shafee R., Narayan R., McClintock J. E., 2008, ApJ
Shimura T., Takahara F., 1995a, ApJ, 440, 610
Shimura T., Takahara F., 1995b, ApJ, 445, 780
Stern B. E., Begelman M. C., Sikora M., Svensson R., 1995, MNRAS, 272, 291
Suleimanov V., Poutanen J., Werner K., 2012, A&A, 545, A120
Sunyaev R. A., Titarchuk L. G., 1980, A&A, 86, 121
Takahashi H. R., Ohsuga K., 2015, PASJ, 67, 60
Tanaka Y., Nandra K., Fabian A. C., Inoue H., Otani C., Dotani T., Hayashida K., Iwasawa K., Kii T., Kunieda H., Makino F., Matsuoka M., 1995, Nature, 375, 659
Titarchuk L., Lyubarskij Y., 1995, ApJ, 450, 876
Turolla R., Zane S., Titarchuk L., 2002, ApJ, 576, 349
White N. E., Stella L., Parmar A. N., 1988, ApJ, 324, 363
Yuan F., Narayan R., 2014, ARAA, 52, 529
Zane S., Turolla R., Nobili L., Erna M., 1996, ApJ, 466, 871
Zhang S. N., Cui W., Chen W., 1997, ApJL, 482, L155
Zhu Y., Davis S. W., Narayan R., Kulkarni A. K., Penna R. F., McClintock J. E., 2012, MNRAS, 424, 2504
Zhu Y., Narayan R., Sądowski A., Psaltis D., 2015, MNRAS, 451, 1661